NuSTAR observations of the bullet cluster: constraints on inverse compton emission

Wik, Daniel R.; Hornstrup, Allan; Molendi, S.; Madejski, G.; Harrison, F. A.; Zoglauer, A.; Grefenstette, B. W.; Gastaldello, F.; Madsen, K. K.; Westergaard, Niels Jørgen Stenfeldt

Total number of authors:
19

Published in:
Astrophysical Journal

Link to article, DOI:
10.1088/0004-637X/792/1/48

Publication date:
2014

Document Version
Publisher's PDF, also known as Version of record

The Astrophysical Journal, 792:48 (24pp), 2014 September 1 doi:10.1088/0004-637X/792/1/48

NuSTAR OBSERVATIONS OF THE BULLET CLUSTER: CONSTRAINTS ON INVERSE COMPTON EMISSION

Daniel R. Wik[1,2], A. Hornstrup[3], S. Molendi[4], G. Madejski[5], F. A. Harrison[6], A. Zoglauer[7], B. W. Grefenstette[6], F. Gastaldello[4], K. K. Madsen[6], N. J. Westergaard[3], D. D. M. Ferreira[3], T. Kitaguchi[8], K. Pedersen[3], S. E. Boggs[7], F. E. Christensen[3], W. W. Craig[7,9], C. J. Hailey[10], D. Stern[11], and W. W. Zhang[1]
[1] Astrophysics Science Division, NASA/Goddard Space Flight Center, Greenbelt, MD 20771, USA; daniel.r.wik@nasa.gov
[2] Department of Physics and Astronomy, Johns Hopkins University, Baltimore, MD 21218, USA
[3] DTU Space, National Space Institute, Technical University of Denmark, Elektrovej 327, DK-2800 Lyngby, Denmark
[4] IASF-Milano, INAF, Via Bassini 15, I-20133 Milano, Italy
[5] Kavli Institute for Particle Astrophysics and Cosmology, SLAC National Accelerator Laboratory, Menlo Park, CA 94025, USA
[6] Cahill Center for Astronomy and Astrophysics, California Institute of Technology, Pasadena, CA 91125, USA
[7] Space Sciences Laboratory, University of California, Berkeley, CA 94720, USA
[8] RIKEN Nishina Center, 2-1 Hirosawa, Wako, Saitama 351-0198, Japan
[9] Lawrence Livermore National Laboratory, Livermore, CA 94550, USA
[10] Columbia Astrophysics Laboratory, Columbia University, New York, NY 10027, USA
[11] Jet Propulsion Laboratory, California Institute of Technology, Pasadena, CA 91109, USA
Received 2014 March 11; accepted 2014 July 17; published 2014 August 13

ABSTRACT

The search for diffuse non-thermal inverse Compton (IC) emission from galaxy clusters at hard X-ray energies has been undertaken with many instruments, with most detections being either of low significance or controversial. Because all prior telescopes sensitive at $E > 10$ keV do not focus light and have degree-scale fields of view, their backgrounds are both high and difficult to characterize. The associated uncertainties result in lower sensitivity to IC emission and a greater chance of false detection. In this work, we present 266 ks *NuSTAR* observations of the Bullet cluster, which is detected in the energy range 3–30 keV. *NuSTAR*'s unprecedented hard X-ray focusing capability largely eliminates confusion between diffuse IC and point sources; however, at the highest energies, the background still dominates and must be well understood. To this end, we have developed a complete background model constructed of physically inspired components constrained by extragalactic survey field observations, the specific parameters of which are derived locally from data in non-source regions of target observations. Applying the background model to the Bullet cluster data, we find that the spectrum is well—but not perfectly—described as an isothermal plasma with $kT = 14.2 \pm 0.2$ keV. To slightly improve the fit, a second temperature component is added, which appears to account for lower temperature emission from the cool core, pushing the primary component to $kT \sim 15.3$ keV. We see no convincing need to invoke an IC component to describe the spectrum of the Bullet cluster, and instead argue that it is dominated at all energies by emission from purely thermal gas. The conservatively derived 90% upper limit on the IC flux of 1.1×10^{-12} erg s^{-1} cm^{-2} (50–100 keV), implying a lower limit on $B \gtrsim 0.2$ μG, is barely consistent with detected fluxes previously reported. In addition to discussing the possible origin of this discrepancy, we remark on the potential implications of this analysis for the prospects for detecting IC in galaxy clusters in the future.

Key words: galaxies: clusters: general – galaxies: clusters: individual (Bullet cluster) – intergalactic medium – magnetic fields – radiation mechanisms: non-thermal – X-rays: galaxies: clusters

Online-only material: color figures

1. INTRODUCTION

A number of observations, mainly at radio frequencies, have established that relativistic particles and magnetic fields are part of the intracluster medium (ICM) of galaxy clusters (e.g., Govoni & Feretti 2004). The large (∼Mpc) scale, diffuse structures known as radio halos and relics are produced by relativistic electrons spiraling around ∼μG magnetic fields. The synchrotron emission is a product of both the particle and magnetic field energy densities, the latter of which is not well constrained globally from these or other observations. However, the electron population can be independently detected through inverse Compton (IC) scattering off of ubiquitous cosmic microwave background (CMB) photons, which are up-scattered to X-ray energies and may be observable if the electron population is sufficiently intense (Rephaeli 1979). For single electrons or populations with power-law energy distributions, the ratio of IC to synchrotron flux gives a direct, unbiased measurement of the average magnetic field strength B in the ICM of a cluster. The magnetic field plays a potentially important role in the dynamics and structure of the ICM, such as in sloshing cool cores where B may be locally amplified so that the magnetic pressure is comparable to the thermal pressure (ZuHone et al. 2011). Detections of IC emission, therefore, probe whether the non-thermal phase is energetically important or, particularly if the average magnetic field is large, whether it is sizable enough to affect the dynamics and structure of the thermal gas.

The quest for the detection of IC emission associated with galaxy clusters began with the launch of the first X-ray sensitive sounding rockets and satellites, although the origin of extended, ∼keV X-rays from clusters was soon recognized to be thermal (e.g., Solinger & Tucker 1972; Mitchell et al. 1976). Even so, in clusters with radio halos or relics, IC emission *must* exist at some level, since the CMB is cosmological. Thermal X-ray photons are simply too numerous at $E \lesssim 10$ keV for a reliable detection of the IC component; at higher energies, however, the bremsstrahlung continuum falls off exponentially, allowing the non-thermal IC emission to eventually dominate and produce

"excess" flux in the spectrum. While the first IC searches with *HEAO-1* yielded only upper limits, and thus lower limits on the average strength of ICM magnetic fields, $B \gtrsim 0.1\ \mu$G (Rephaeli 1987; Rephaeli & Gruber 1988), the next generation of hard X-ray capable satellites—*RXTE* and *Beppo-SAX*—produced detections in several clusters, although mostly of marginal significance (for a review, see, e.g., Rephaeli et al. 2008). The most recent observatories—*Suzaku* and *Swift*—however, have largely failed to confirm IC at similar levels (Ajello et al. 2009, 2010; Wik et al. 2012; Ota et al. 2014). One exception is the Bullet cluster (a.k.a. 1E 0657−56, RX J0658−5557), although the detection significance of the non-thermal component is marginal in both the *RXTE* and *Swift* data alone.

The *RXTE* observation of the Bullet cluster's had X-ray emission was not very constraining, but the overall spectrum from the PCA and HEXTE instruments, fit jointly with *XMM-Newton* MOS data, favored a non-thermal tail at not quite 3σ significance (Petrosian et al. 2006). A two-temperature model fit the data equally well, but the higher temperature component had a nearly unphysically high temperature (∼50 keV) for a large (10%) fraction of the total emissivity. In a similar analysis, the *XMM-Newton* data were simultaneously fit with a spectrum from the *Swift* BAT all sky survey, and the non-thermal component was confirmed at the 5σ confidence level (Ajello et al. 2010). However, a two-temperature model technically did a better job of describing the spectra, although the secondary temperature component was very low (1.1 keV), causing the authors to reject this interpretation. While this low temperature component is certainly not physical, the fact that a model can fit the data so well when an extra component is added solely at low energies indicates that the non-thermal component is not being strongly driven by the BAT data. Further confirmation of an IC component in the Bullet cluster is clearly necessary to rule out a purely thermal description of the hard band emission and uphold the implied magnetic field strength of $\sim 0.16\ \mu$G.

The intriguing evidence for a non-thermal excess at hard energies coupled with its smaller angular size makes the Bullet cluster an ideal galaxy cluster target for the *NuSTAR* X-ray observatory (Harrison et al. 2013). *NuSTAR* is the first focusing hard X-ray telescope with a bandpass between 3 and 80 keV and is the first telescope with the ability to focus X-rays in the hard X-ray band above 10 keV. It has an effective area at 30 keV of 2×110 cm^2 and imaging half power diameter of $58''$. While the effective area is somewhat lower than that of previous instruments, the focusing capability vastly reduces the background level and its associated uncertainties. Collimators on board *RXTE*, *Beppo-SAX*, and *Suzaku* have $\sim 1^\circ$ full fields of view (FOVs), out to where their responses fall to zero. Such large FOVs are more likely to unknowingly include emission from a bright source or sources unassociated with the target, while the equivalent region of the Bullet cluster within *NuSTAR* spans $\sim 100\times$ less solid angle on the sky. Also, for clusters that fit well within *NuSTAR*'s $\sim 13' \times 13'$ FOV, simultaneous offset regions can be used to precisely characterize the background to an extent not possible with collimated instruments.

We describe the two *NuSTAR* observations and their generic processing in Section 2. In Section 3, the modeling of the background and its systematics and the overall flux calibration are briefly described (see Appendices A and B for details). We examine hard band images and the character of the global spectrum in Section 4. Finally, the implications of these results are discussed in Section 5. We assume a flat cosmology with $\Omega_M = 0.23$ and $H_0 = 70$ km s^{-1} Mpc^{-1}. Unless otherwise stated, all uncertainties are given at the 90% confidence level.

Table 1
Observations

ObsID	Optical Axis Location		Exposure Time	
	α(J2000) (deg)	δ(J2000) (deg)	Raw[a] (ks)	Cleaned (ks)
70001055002	104.63207	−55.924552	231	126
70001056002	104.53211	−55.919636	287	140

Note. [a] Includes Earth occultations.

2. OBSERVATIONS AND STANDARD PROCESSING

The Bullet cluster was observed by *NuSTAR* in two epochs. The optical axis fell near the centroid of the large-scale X-ray emission in the first observation and near the western shock driven by the bullet subcluster in the second. The first pointing was carried out over a little under 3 days, 2012 October 18–20, for a total unfiltered exposure of 231 ks. For the second pointing, the Bullet cluster was observed for a slightly longer raw exposure of 287 ks from 2012 November 1–4. To filter the events, standard pipeline processing (HEASoft v6.13 and NuSTARDAS v1.1.1) was applied along with stricter criteria regarding passages through the South Atlantic Anomaly (SAA) and a "tentacle"-like region of higher activity near part of the SAA; in the call to the general processing routine that creates Level 2 data products, `nupipeline`, the following flags are included: `SAAMODE=STRICT` and `TENTACLE=yes`. These additional flags reduce the cleaned exposure time, given in Table 1, by $\lesssim$10% from what it would otherwise be, but the flags also reduce background uncertainties. No strong fluctuations are present in light curves culled from the cleaned events, suggesting a stable background, so no further time periods were excluded.

From the cleaned event files, we directly extract images like those shown in Figure 1 and light curves using `xselect`, create exposure maps using `nuexpomap`, and extract spectra and associated response matrix (RMF) and auxiliary response (ARF) files using `nuproducts`. The call to `nuproducts` includes `extended=yes`, most appropriate for extended sources, which weights the RMF and ARF based on the distribution of events within the extraction region, assuming that to be equivalent to the true extent of the source. Although the effective smoothing of the source due to the point-spread function (PSF) is not folded in with the weighting, the relatively narrow FWHM of $\sim 18''$ lessens the impact of this omission. The response across a given detector is largely uniform, so the RMFs of the four detectors are simply averaged by the weighted fraction each detector contributes to a region. In addition to the mirror response, the ARF includes low energy absorption in the detectors (due to a CdZnTe dead layer and platinum electrodes) and is also "corrected" to a canonical power-law Crab spectrum of photon index 2.1 and normalization 9.7 photons s^{-1} cm^{-2} keV^{-1} at 1 keV. The remaining products necessary to analyze the spectra—background spectra and a PSF-corrected flux calibration—are tailored for this analysis and described in Section 3.

3. BACKGROUND MODELING AND FLUX CALIBRATION

One of *NuSTAR*'s pioneering technologies, at least for an astrophysics X-ray mission, is the separation of its optics and

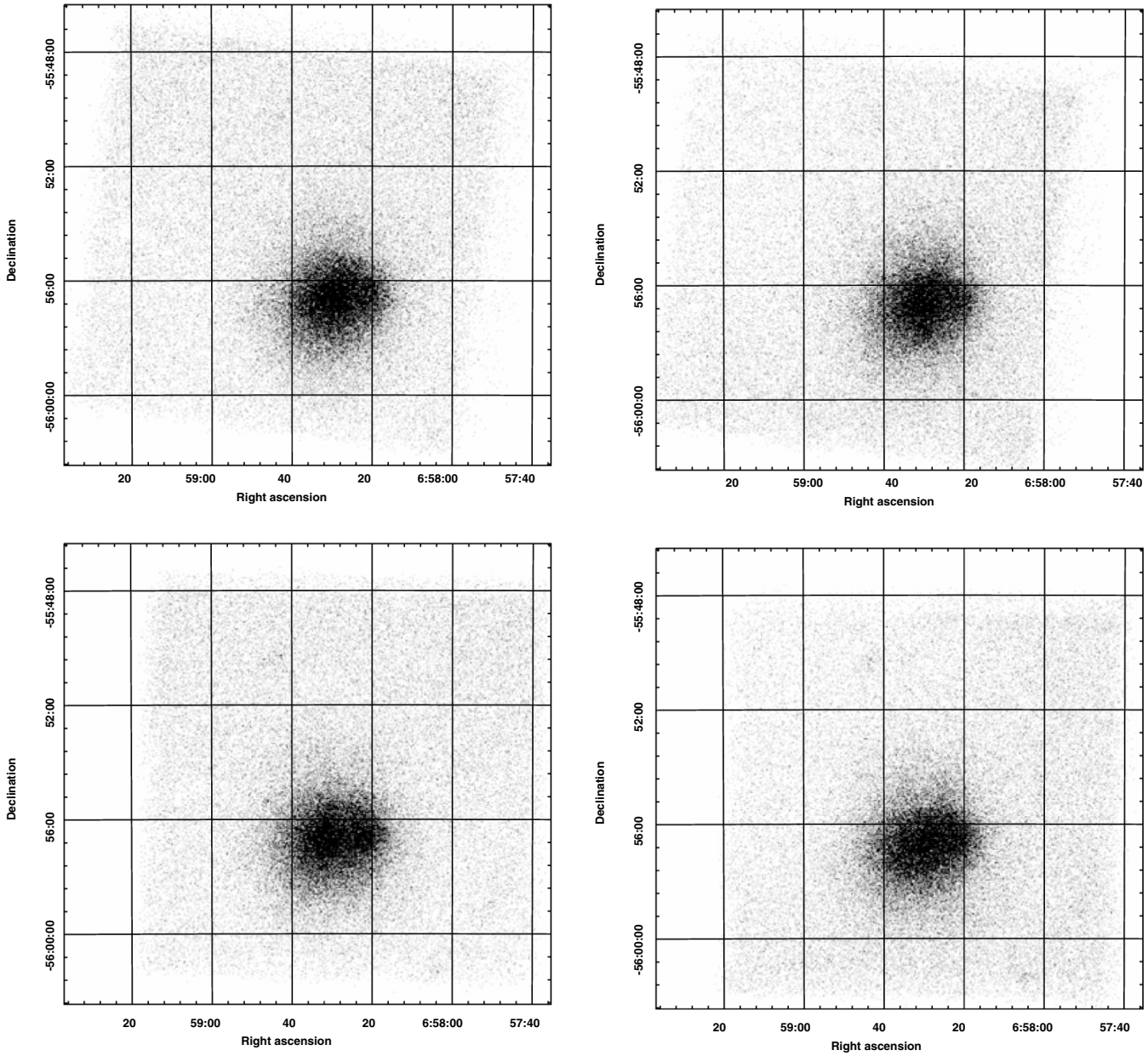

Figure 1. Cleaned events projected in sky coordinates from 3–20 keV; pixels with no events are displayed as white while pixels with 1 or $\geqslant$2 events are displayed as gray or black, respectively. Top row: ObsID 700055002 images; Bottom row: ObsID 700056002 images. The left and right columns show the data from the A and B telescopes, respectively.

focal plane modules by an open mast structure that was extended after launch. The telescope is thus open and subject to stray light, which dominates the background at low energies and creates a spatial gradient across the FOV. The stray light must be distinguished from the instrumental background, which varies from detector to detector but is otherwise spatially uniform, in order to use local background regions for any source region. Also, because the PSF scatters some emission outside our extraction region, we must estimate the fraction of the emission collected within the region by convolving the cluster's true spatial distribution with the PSF, which varies with off-axis angle. Our solution to these challenges is outlined below.

3.1. Background

As is typical, the background has both intrinsic and extrinsic components, which for *NuSTAR* vary in relative importance both spectrally, spatially, and somewhat temporally. For faint sources where the background is a significant fraction of the source counts, it is to some degree inappropriate to naively extract and rescale a spectrum from elsewhere in the FOV to use as a background. However, because the background components are reasonably well understood and stable (Figure 2), we can model its instantaneous composition from source-free regions and, using what we know about the spatial variations of each component, extrapolate that model to the source region. The model consists of four components, which combine to fully describe the background:

$$B_d(E, x, y) = I_d(E) + A_d(E, x, y) + S_d(E) + f_d(E, x, y), \quad (1)$$

where the total background $B_d(E, x, y)$ is given for each detector d at energy E and detector pixel position x, y. The definition and physical origin of the individual components are

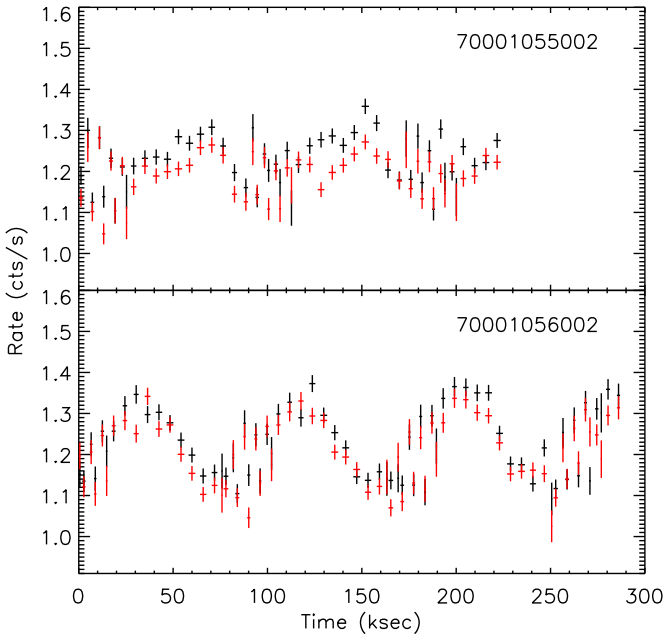

Figure 2. Full FOV and energy (1.6–160 keV) light curves for the two observations and telescopes (A: black; B: red/gray). The background dominates the total rate and is stable, modulo diurnal variations primarily caused by the position of the SAA relative to observing windows (i.e., when the SAA is on the same side of the Earth as the Bullet cluster).

(A color version of this figure is available in the online journal.)

briefly described below; for details on the specific models and how the background is actually fit with them, see Appendix A. These components are all identified in the spectra shown in Figure 10, and it may benefit the reader to refer to it and the following section simultaneously.

3.1.1. Components

Internal $I_d(E)$. The radiation environment of *NuSTAR*'s orbit leads to a roughly flat background across all energy channels. An underlying featureless continuum is produced primarily, but probably not entirely, by high energy gamma rays which either pass through the anti-coincidence shield and Compton scatter in the detector or scatter untriggered in the shield itself. The remainder of the internal background consists of various activation and fluorescence lines, which are mostly resolved and only dominate the background between 22–32 keV. Above these energies weaker lines are still present, but the continuum dominates. The spatial distribution across a given detector d is uniform, so there is no dependence on pixel location x, y, only on energy E, which varies slightly for each detector. More details can be found in Appendix A.1

Aperture Stray Light $A_d(E, x, y)$. Because the space between the optics and focal plane benches is not fully baffled, a series of aperture stops protrude from the focal plane bench to block unfocused X-rays from striking the detectors (for a diagram of this geometry, see Figure 9). Due to technical implementation limitations, the aperture stop does not exclude 100% of the stray light, leaving a few degree window centered on each mirror module. The amount of sky visible to any given detector pixel varies as a function of its x, y position. Since the cosmic X-ray background (CXB) is roughly uniform on large scales, the intensity $A_d(E, x, y)$ is proportional to the solid angle visible through the aperture stops; we refer to this component as the "Aperture" background hereafter. The CXB spectral shape is consistent with that found by previous missions, and we adopt the canonical *HEAO-1 A2* spectral model, valid from 3–60 keV (Boldt 1987). Due to cosmic variance, the precise normalization for any given observation should be measured intrinsically (see Appendix B for details).

Scattered and Reflected Stray Light $S_d(E)$. Besides direct exposure to sources of stray light, the open geometry of the spacecraft is susceptible to reflected and scattered X-rays from the entire sky. One possible reflecting surface—along with many other parts of the observatory, including the mast—is the backside of the aperture stops, which are clearly visible to the detectors. There are three potential sources of reflected emission: the CXB, the Earth, and the Sun. Because such a large fraction of the sky is visible to the backside of the aperture stops, they are capable of reflecting a contribution of 10%–20% of the total "Aperture" CXB emission despite their smaller solid angle and low reflectivity. Assuming the spectrum is unchanged and uniformly illuminates the detectors, this extra emission simply adds to that coming through the aperture stops and can be included in the $A_d(E, x, y)$ term. Emission from the Sun ("Solar"), and potentially the Earth's albedo, is much softer and also much more variable. During episodes of high solar activity, the background below $E \sim 5$–6 keV will be dominated by a $\sim$1 keV thermal spectrum of solar abundance, but even during less active periods this component accounts for $\sim$40% of the $E \lesssim 5$ keV total. The "Solar" emission is only present when the satellite is illuminated by the Sun, so there is no doubt as to its origin. There are also some weak fluorescence lines from material elsewhere on the spacecraft, such as the mast, that contribute to the background, although their origin and contribution is still under active investigation. For now we include them as low energy lines in the $I_d(E)$ term. The "Solar" component primarily makes up the $S_d(E)$ term, which has no spatial dependence beyond offsets between detectors. A less trivial spatial dependence would not be surprising, but it is too weak to be inferred at present.

Focused Cosmic Background $f_d(E, x, y)$. Unlike the above components, there always exists an inherent "background" from other unresolved foreground/background sources within the FOV that are not of primary scientific interest. While subdominant at all energies, the focused CXB ("fCXB") contributes noticeably below 15 keV—having roughly 10% the flux of the "Aperture" CXB—with a slightly softer spectrum than the "Aperture" CXB since it has been modulated by the mirror effective area, which begins to decline above 10 keV. It varies spatially, although not predictably, due to cosmic variance.

3.1.2. Systematic Uncertainties

Although we directly measure the contribution of each component, we do not do so with infinite precision or accuracy. Inaccurately estimated systematic offsets can easily lead to "detections," especially when the associated precision of a component is overestimated. Faint spectral components, such as IC emission in galaxy clusters, fall into in this category since they tend to reside in background-dominated regimes. Therefore, we must have some sense of the systematic uncertainty intrinsic to the background, and as much as possible to each component of the background. For some components, like the internal background, the systematic uncertainty could in theory be arbitrarily close to 0%. In practice, of course, uncertainties of less than a few percent are difficult to achieve. Components with a cosmic origin, however, have systematic uncertainty floors due to their very natures. While these uncertainties are sometimes large, they may also be well known, as in the case of the CXB.

At higher ($E > 40$ keV) energies, where the $I_d(E)$ term strongly dominates, performing the background fitting procedure outlined in Appendix B on the first-pass ECDFS survey fields results in an accurate reconstruction of the background level with a standard deviation of <3% after accounting for the effect of statistical fluctuations. Although the real uncertainty may be smaller, the large statistical uncertainties due to the shorter exposure time (~40 ks/field) make it difficult to surmise with greater precision. We adopt a conservative uncertainty of 3% for the entire energy range. Because much of this regime is dominated by lines, whose normalizations have independent systematic uncertainties that are dwarfed by their statistical uncertainties, a global shift up or down maximizes this background's impact on fits to the cluster spectrum.

The shape of the CXB spectrum has been well-measured by other missions (e.g., Türler et al. 2010), and although it may vary on small scales, the larger scales relevant to the $A_d(E, x, y)$ term are unlikely to exhibit noticeable deviations from the average spectrum. The overall normalization, however, depends critically on the number of more rare, brighter sources, which varies from one location to another on the sky. Because we have no way to exclude the brightest sources, even the variance on large scales (0.3–10 deg^2 pixel^{-1} over a total solid angle of 37.2 deg^2) can be high. We can eliminate much of this uncertainty by directly measuring it in the non-source regions of an observation. This technique is especially powerful thanks to the strong correlation of the "Aperture" normalization between source and non-source regions. Each CXB point source produces an aperture-shaped (circular aperture stop opening modulated by any fraction blocked by the optics bench, see Figure 9) "plateau" of emission across the detectors, so many pixels are illuminated by the same sources, especially those pixels that are nearby to each other. However, background and source regions will not contain all the same CXB sources, so a residual uncertainty remains.

We estimate this uncertainty by realistically simulating CXB point sources and measuring the incident flux at different x, y locations in the detector plane. While the "Aperture" normalization is directly measured in background regions, its normalization in the Bullet cluster extraction region may differ due to cosmic variance. Source fluxes are drawn from the 2–8 keV log N–log S distribution of Kim et al. (2007), randomly positioned on the sky, and projected onto the detectors. Over 1000 realizations, the "Aperture" CXB normalization in the cluster and background regions is found to agree to within 8% (1σ). We take this value as the systematic uncertainty inherent in applying the $A_d(E, x, y)$ term as measured in background regions to the cluster extraction region.

In principle, scattered and reflected X-rays (contributing at the lowest energies) should be nearly perfectly correlated between all pixels, even if their spatial distribution is not necessarily uniform. Because we do not know exactly where the scattering is taking place, we cannot predict the appearance of this emission like we can for the "Aperture" background. It does not appear to be flat; independent fits of spectra from the various detectors give different normalizations. Unfortunately, it is not yet feasible to empirically determine the shape any more finely than that at this time. Based on the same exercise used to constrain the uncertainty of the $I_d(E)$ term, the $S_d(E)$ term's systematic uncertainty is found to be 10% (1σ).

For the "fCXB" emission modeled in the $f_d(E, x, y)$ term, we can apply a straightforward shorthand estimate of cosmic variance, consistent with the method used for the "Aperture" component but based on an empirical instead of a simulated estimate of the variance. We assume a conservative point source detection threshold of 3×10^{-13} erg s^{-1} cm^{-2} (20–30 keV), below which individual sources would not be obvious embedded within the cluster emission (see Section 4.1 for details). The variance scales as $\sigma_{\rm CXB}/I_{\rm CXB} \propto \Omega^{-0.5} S_{\rm cut}^{0.25}$, where Ω is the solid angle on the sky and $S_{\rm cut}$ is the flux limit for excised point sources. For our elliptical source region, shown in Figure 3, $\Omega = 31$ arcmin^2. We can estimate the variance in our observation relative to another measurement assuming a log N–log S relation of $N(S) \propto S^{-1.5}$. Using the *HEAO-1 A2* estimate (Shafer 1983; Barcons et al. 2000; Revnivtsev et al. 2003) with $\Omega = 15.8$ deg^2, $S_{\rm cut}$(20–30 keV) $= 2.1 \times 10^{-11}$ erg s^{-1} cm^{-2}, and $\sigma_{\rm CXB}/I_{\rm CXB} = 2.8\%$ (1σ), we find a variance and thus systematic uncertainty of ~42% (1σ) for our extraction region.

3.2. Flux Calibration

Since we want the total cluster flux, to first order we could simply use as large a region as possible and assume that includes all the emission. However, the PSF wings cause a fraction of the flux to get redistributed far from its true origin on the sky, which results in some emission being scattered beyond the FOV as defined by the detectors. Detector gaps also miss flux, and one just happens to fall across the brightest part of the Bullet during the second observation. These effects require careful correction so that the exposure across the field is accurate.

As mentioned in Section 2, the ARF for an extended source is created by averaging the vignetting function across the region, weighted by the distribution of events. Extended source ARFs are not additionally corrected for any source emission scattered out of the region through the wings of the PSF. To get a proper total flux for the Bullet cluster spectrum, we must take the PSF and estimate the fraction of the total emission captured inside the region. This task is not entirely trivial since not only does the PSF shape vary with off-axis angle, but the off-axis angle varies for any given position on the sky over the course of an observation. Normally, one could neglect the variation in shape, as it only becomes a measurable effect for large ($\gtrsim 3'$) off-axis angles. Because the placement of the cluster in the second observation results in large off-axis angles for its eastern parts, we include these minor adjustments to the PSF shape. Following Nynka et al. (2013), we can construct composite or effective PSFs for our particular observations across the entire cluster, so that each position has an appropriate PSF associated with it. Now armed with a set of position-dependent PSFs (but not energy-dependent), the flux in the wings can be directly computed. Note that the PSF varies weakly as a function of energy; below ~8 keV, the FWHM is up to 10% broader than it is at higher energies, although the encircled energy fraction within a radius of $\gtrsim 1'$ agrees to within a few percent at all energies. The latter behavior justifies our use of an energy-independent PSF.

Ideally, we would like to take the true flux distribution from the cluster and convolve it with the PSFs to estimate the redistributed fraction, but above ~7 keV *NuSTAR* is the only telescope capable of making a reliable image. To estimate the fraction of the total flux in the 3–20 keV energy range within our spectral extraction region (within the ellipse shown in the upper left panel of Figure 3), we generate PSFs in a 25×28 grid—each position separated by 1 FWHM of 18″—and roughly fit them to the A and B telescope images. The extraction region encompasses 95% of the intrinsic flux from the cluster, and a net ~5% of that is scattered out of the region by the PSF. Thus, in

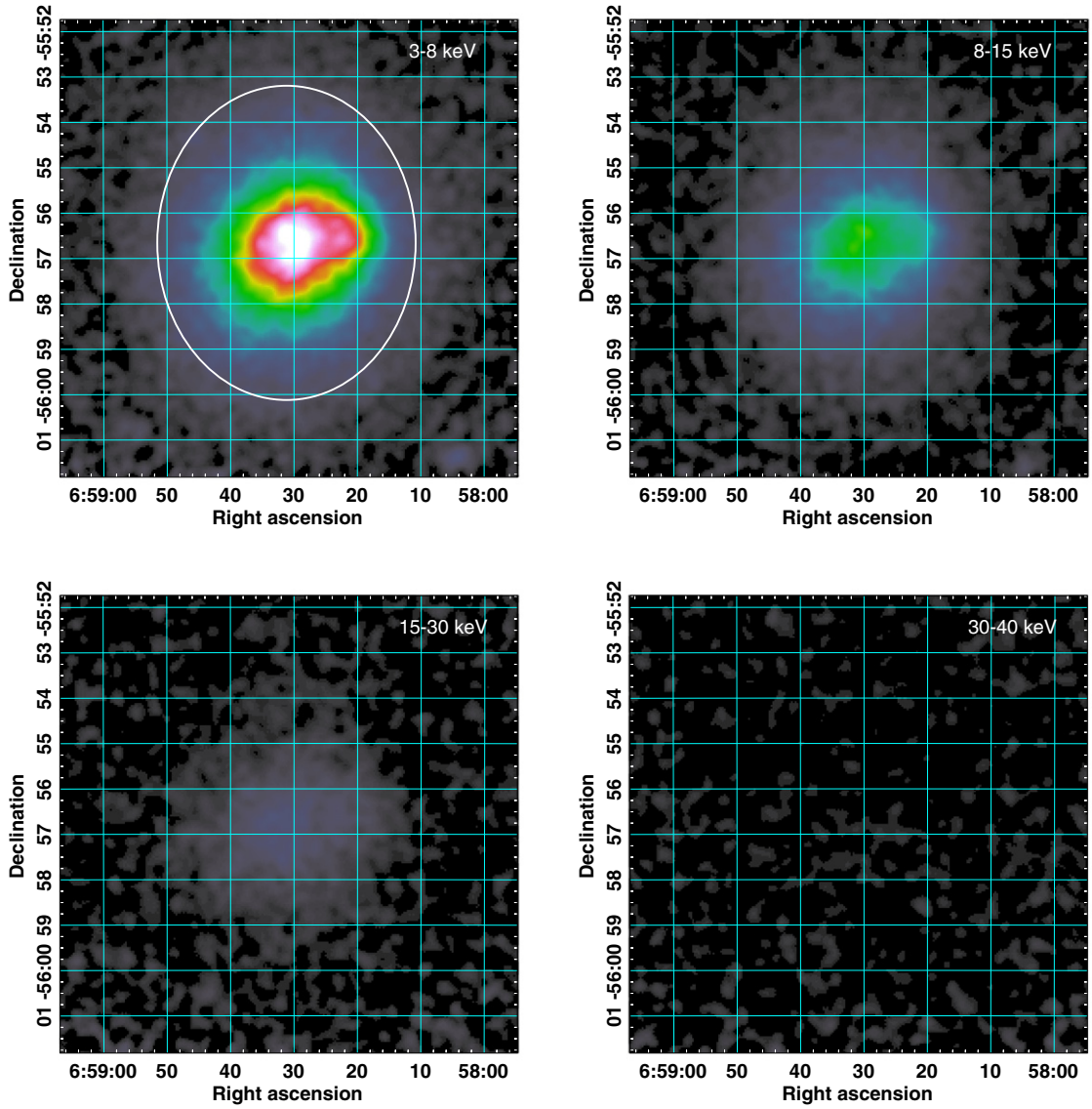

Figure 3. Background-subtracted and exposure-corrected images combined from both observations and telescopes. Images are presented on a linear scale from 0 counts s^{-1} $pixel^{-1}$ (black) to 5×10^{-5} counts s^{-1} $pixel^{-1}$ (white). The energy band of each image is shown clockwise from top left: 3–8 keV, 8–15 keV, 30–40 keV, and 15–30 keV. The ellipse in the top left panel indicates the region from which spectra are extracted. Images are smoothed with a uniform Gaussian kernel of $\sigma = 12\farcs3$ (5 pixels). Although fewer cluster counts are detected at higher energies, no obvious change in morphology occurs relative to the 3–8 keV image, which is dominated by thermal photons.

(A color version of this figure is available in the online journal.)

terms of total cluster emission, our spectrum captures ∼90% of the total 3–20 keV flux. When comparing to past observations, our quoted model normalizations and fluxes would then be 10% lower; however, the overall effective area given in the calibration used here is ∼15% lower than that needed to match with *Swift* XRT and *XMM-Newton* EPIC fluxes, which means our fluxes should also be decreased 15% (this adjustment is present in later `CALDB` releases). Since these corrections roughly cancel out, and given the uncertain nature of absolute calibration between telescopes, we do not further adjust the normalizations and fluxes derived from model fits to the spectra.

4. IMAGES AND SPECTRA

4.1. Images

Although the goal of this paper is to determine the character of the hardest emission in the cluster, we must first confirm that no reasonably bright point sources contaminate that emission. Unlike all previous observatories, *NuSTAR*'s unprecedented spatial resolution at hard energies makes a task heretofore impossible as simple as examining the images.

The pipeline-filtered event files are sufficiently processed to produce images, which can be done in arbitrary energy bands by further filtering on the PHA column in, e.g., `xselect`. However, calibrated images also require exposure-correction and background-subtraction; the necessary images are generated from `nuexpomap` and `nuskybgd`, respectively. The latter is not part of the *NuSTAR* software distribution, but was developed independently as part of this work. (see Appendices A and B). We create exposure maps at single energies for each band, which roughly correspond to the mean emission-weighted energy of the band. To mosaic the two epochs along with the data from both telescopes, we also need to correct for offsets due to the ∼5″ uncertainty in the reconstructed astrometry. No obvious point

sources appear within the FOV, so we estimate the necessary shifts using the global distribution of the cluster emission and find slight offsets of 0–3 pixels relative to the first epoch's A telescope astrometry. Because the 2.″46 pixels significantly oversample the PSF, the final images are smoothed by 5 pixels, more consistent with the PSF's FWHM of ∼18″.

Images in four energy bands (top: 3–8 keV, 8–15 keV; bottom: 15–30 keV, 30–40 keV) are presented in Figure 3. The white ellipse shows the extraction region for spectra discussed in Section 4.2. From 3–8 keV, the cluster resembles the *Chandra* or *XMM-Newton* images blurred by the larger *NuSTAR* PSF, except that the "bullet" to the west is relatively de-emphasized since it is composed of cooler ($\lesssim$7 keV) gas than is the main subcluster ($kT \sim 14$ keV) and *NuSTAR*'s response is more sensitive to harder emission in this band. Above 8 keV, the "bullet" essentially disappears, although the halo of shocked gas surrounding it is clearly visible. The cluster begins to approach the level of the background above 15 keV, and above 30 keV whatever detectable emission remains is highly background-dominated. While the overall morphology changes slightly with energy—a subject of a future paper—it does not deviate appreciably from what one would expect extrapolating a temperature map measured at energies <8 keV, suggesting the origin of the $E > 8$ keV emission is also mostly, if not entirely, thermal as well.

Most critically, there is no indication of a background active galactic nucleus (AGN) whose emission could masquerade as the non-thermal emission we are searching for. The Bullet cluster is generally free of bright point sources; the contribution of obvious point source emission in the 0.8–4 keV band from a 0.5 Ms *Chandra* mosaic (courtesy M. Markevitch) is ∼0.9% of the total cluster emission, or a flux of roughly 7×10^{-14} erg s^{-1} cm^{-2}. Of course, considering these sources alone does not protect us from contamination by absorbed or very hard sources. While there are no bright point sources in our images, *NuSTAR*'s large PSF makes it more difficult to distinguish point sources embedded within the diffuse cluster emission. We can estimate the approximate brightness of point sources that we would be able to identify visually by adding a fake source to the data and noting the flux above which the source becomes readily apparent. The resulting flux limit is likely higher than what might be achieved with `wavdetect` or some other point source identification method, but relying on simple visual inspection of images is straightforward and sufficient for these purposes. In images covering the entire relevant energy band (3–40 keV), point sources would be clearly identified within a radius of ∼1′ if they are $\gtrsim$5% of the total cluster flux and $\gtrsim$1% outside this radius, corresponding to flux limits of 2–9 $\times 10^{-13}$ erg s^{-1} cm^{-2}. At higher energies, the signal to noise rapidly declines; in the 20–30 keV band point sources only become obvious when they have $\gtrsim$20% of the cluster emission at those energies, or $\gtrsim 3 \times 10^{-13}$ erg s^{-1} cm^{-2}. These limits are roughly comparable, with the 5% limit above translating to a flux in the 20–30 keV band of $\gtrsim 2 \times 10^{-13}$ erg s^{-1} cm^{-2}, assuming a power-law spectrum with a typical photon index of 1.8. Note that the entire FOV of *NuSTAR* is at least a factor of two smaller than the effective PSF of the *Suzaku* HXD-PIN and *Swift* BAT instruments, further reducing the comparative chance of a point source contaminating the hard X-ray spectrum.

4.2. Spectrum

Figure 4 displays the four raw spectra extracted with `nuproducts` from the elliptical region illustrated in Figure 3.

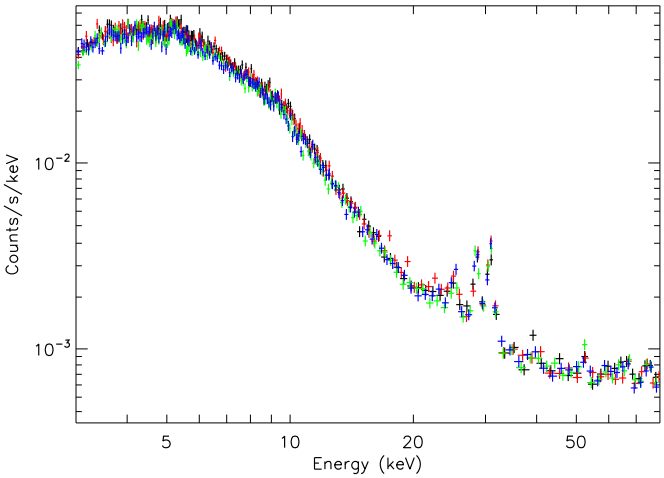

Figure 4. Raw spectra from the region indicated in the top left panel of Figure 3, grouped into 15σ bins for clarity. ObsID 700055002 spectra are in black (telescope A) and red (B) and ObsID 700056002 spectra are in green (A) and blue (B). Above ∼20 keV the background dominates each spectrum, causing a flattening and the appearance of lines due to instrumental fluorescence and activation from SAA passages.

(A color version of this figure is available in the online journal.)

The consistency between the four spectra demonstrate the very similar effective areas between the two telescopes, the shallow vignetting function below 20 keV (the primary difference between the two epochs is the off-axis angle of the cluster centroid), and the stability of the background (whose dominance coincides with the appearance of strong lines just above 20 keV). The detection of an excess above the thermal tail clearly depends critically on the reproducibility of the background. Via the procedure discussed in detail in Appendices A and B, we have an empirical model for what the background emission should be in this region, based on blank field observations, which has been fit to non-source regions from these observations. This is our best guess for the background spectrum of each observation and telescope, but it is only the most likely state of the background; the actual background may be somewhat different given systematic and statistical uncertainties. A proper background should mimic the statistical impact of the actual background, having both the same area and exposure time of the source region. Typical backgrounds are often taken from larger regions or longer exposures in order to minimize the impact of statistical fluctuations in background regions that could bias the background level in the source region. However, this procedure underestimates the background-subtracted error per channel since the true background suffers from larger statistical uncertainties, which is important wherever the background dominates.

One solution is to jointly fit the background and source data together, but this requires simultaneously fitting 20 spectra (one source and four background spectra for each of the two telescopes and two observations) each with 3675 unbinnned channels, making it computationally challenging just to find a good fit let alone calculate errors on parameter values. To circumvent this difficulty, we separate the background and source modeling phases but attempt to retain a statistically appropriate treatment of the background. As described in Appendix B, a nominal background model is found for the source region for each epoch and telescope. We then simulate, for the same exposure time, a background for the region from this model using `fakeit` in `XSPEC`, including Poisson fluctuations.

Of course, the resulting background spectra fail to incorporate any systematic offsets from the nominal model, and statistical fluctuations introduced to the spectrum have the potential to bias fit parameters as well.

Although not the only path forward, we choose to simulate many realizations of the four backgrounds, fitting the spectra with each set. This procedure naturally allows systematic uncertainties to be incorporated as well, since the several background component model normalizations can be randomly varied to reflect those uncertainties. Each background thus represents a possible version of the true background, ideally in proportion to the likelihood that it matches the true background. A similar approach was taken to incorporate background systematic uncertainties in Moretti et al. (2011). We assume Gaussian fluctuations about the normalizations of each component with magnitudes given in Section 3.1.2; Appendix B outlines the specific methodology in detail.

For continuum-driven fits on data binned to just above the Gaussian limit (25–30 counts bin^{-1}), the χ^2 statistic is known to be biased, especially for fits using a large number of bins (Leccardi & Molendi 2007; Humphrey et al. 2009). Briefly, the weights w on bins with negative fluctuations are overestimated while bins with positive fluctuations are underestimated, since $w = 1/\sqrt{N}$, so the χ^2 statistic drives the global best-fit model below the data. The model derived from fits to the background spectra, for example, are biased by 2%–3% when χ^2 is used as the fit statistic. To avoid this and similar issues with fitting the Bullet cluster spectra, we use the XSPEC command `statistic cstat`, which applies the W statistic, a Cash-like statistic appropriate for fits with unmodeled background spectra. Bins with no counts have a tendency to confuse the implementation of this statistic in XSPEC, so we also group the spectra such that there are at least 3 counts in each bin in *both* data and background spectra.

4.2.1. Models

Armed with a reliable way to deal with the background, we can confidently evaluate the nature of the hardest detectable emission from the Bullet cluster. A strong motivation for these observations was to confirm and better characterize the non-thermal component claimed in Ajello et al. (2010). In clusters with radio halos and relics, such as the Bullet cluster, IC emission—the only diffuse interpretation for a non-thermal tail—must be present at some level. If the IC emission is bright and begins to dominate the spectrum over the thermal emission at a low enough energy, then the spectrum will be trivial to model. The characterization of a weaker IC component, however, depends much more on the model employed to discriminate it from the thermal emission. Of course, our spectrum falls within the latter regime. The range of models considered is somewhat restricted, but appropriate for the data, consisting of single temperature (1T), two temperature (2T), and single temperature plus power-law (T+IC) components. The thermal components are calculated using the version of the Mewe et al. (1995) plasma code implemented in XSPEC.

The 1T model provides the simplest possible description of the spectrum. Emission dominated by isothermal or nearly isothermal gas will be satisfactorily characterized with a single temperature component, since *NuSTAR*'s 0.4 keV FWHM resolution does not allow us to easily separate the Kα line complexes near He-like and H-like Fe at 6.7 and 6.9 keV, respectively. Therefore, we are entirely reliant on the shape of the largely featureless continuum to discern multi-temperature gas. Given our broad bandpass (3–30 keV), the 1T model is unlikely to account for all the truly thermal emission. From *Chandra* and *XMM-Newton*, spatially resolved spectroscopy clearly demonstrates that the ICM contains gas spanning a large range of temperatures (Govoni et al. 2004), which one would expect for an ongoing merger (Tucker et al. 1998). We do not know the true temperature structure, however, only the emission-weighted line-of-sight projected temperature distribution, which is also folded through the effective area and is thus dependent on the calibration and energy band. For the global spectrum, we are not particularly concerned with describing the true temperature structure, since that is not possible. Instead, we wish to accurately represent the part of the temperature distribution seen by *NuSTAR*, which is more heavily weighted toward the hotter regions and thus may not entirely agree with the projected temperature structure measured within a lower energy bandpass. Because thermal continua are fairly featureless, the 2T model will likely encompass the full range of significant gas temperatures. If the IC emission is sufficiently bright, however, then the higher temperature component of the 2T model will be skewed to an unphysically high value. In this case, the T+IC model should provide a better description of the overall spectrum. Although the thermal component would be imperfectly suited to the true thermal distribution, the harder non-thermal component would better capture the spectral shape at higher energies. Note that the statistical power resides at low energies where the majority of counts are, so the non-thermal excess at high energies must be sufficiently strong to overcome the worsening of the fit quality at the low end.

Given that the T+IC model is likely to incompletely describe the thermal part of the spectrum, a 2T+IC model should, in principle, be more accurate and provide a better IC measurement. For this model to be useful, both temperature components must be reasonably constrained by the spectrum. The IC component can then account for excess emission at higher energies without strongly affecting the uncertainties of the 2T parameters, giving one confidence that both thermal and non-thermal properties are truly being captured by the components meant to represent them. In practice, our Bullet cluster spectrum cannot sufficiently constrain the 2T parameters when a non-thermal component is also present. One of the thermal components obtains a very low temperature, which is poorly constrained and unphysical considering its extrapolation to energies below 3 keV. This component acts as a correction to the total thermal spectrum dominantly described by the other temperature component, but because it is poorly constrained the 2T+IC model provides no meaningful improvement over the T+IC model. For this reason, we do not consider it further.

For the non-thermal component of the T+IC model, we fix the power-law photon index to 1.86, the best-fit value found by Ajello et al. (2010). We also allowed the index to be a free parameter, but in nearly all cases the index became steeper ($\Gamma \sim 2.4$), where it was most likely mimicking the lower temperature component of the 2T model. This appropriating of the IC component directly results from the greater statistical power of the counts at the low end of the energy range driving the fit. Although the radio synchrotron spectrum basically agrees with this best-fit index, implying $\Gamma \sim 2.3$ for the IC index (Liang et al. 2000), the electrons producing the radio emission are more energetic (for $B \sim 0.2\ \mu$G, $\gamma \sim 23{,}000$ where γ is the "relativistic gamma" of the electron) than the ones producing the IC ($\gamma \sim 5000$ at 30 keV), so there is no guarantee the photon index would directly follow, and there is good reason to assume

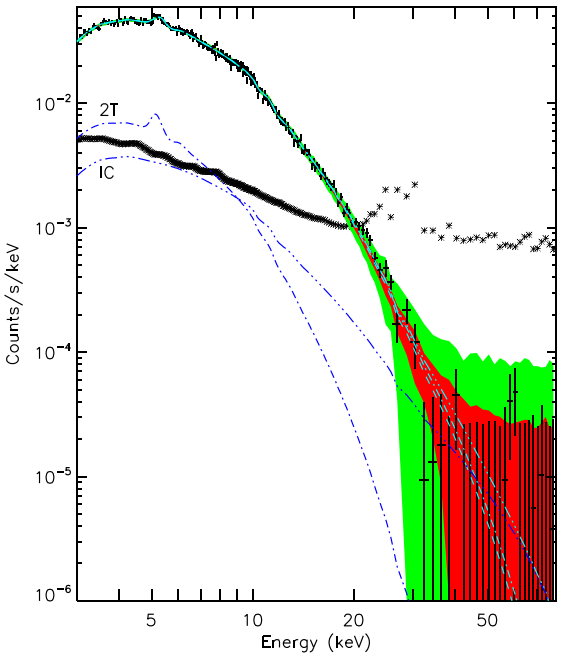

Figure 5. Background-subtracted Bullet cluster spectrum (crosses, using the nominal background model; all spectra from Figure 4 have been combined for clarity) shown together with the background ("*" symbols) and the 1σ (red/dark shaded region) and 3σ (green/light shaded region) effect of background uncertainties relative to the 1T model. The shaded regions indicate the range within which the spectrum might shift due to statistical and systematic fluctuations in the background relative to our nominal background model. The components for the three best-fit models are shown in blue for the 1T, 2T, and T+IC (with Γ fixed at 1.86) cases with the dashed, dot-dashed, and triple dot-dashed lines, respectively. The less dominant component for the 2T and T+IC models are labeled and show the lower temperature component and IC component, respectively.

(A color version of this figure is available in the online journal.)

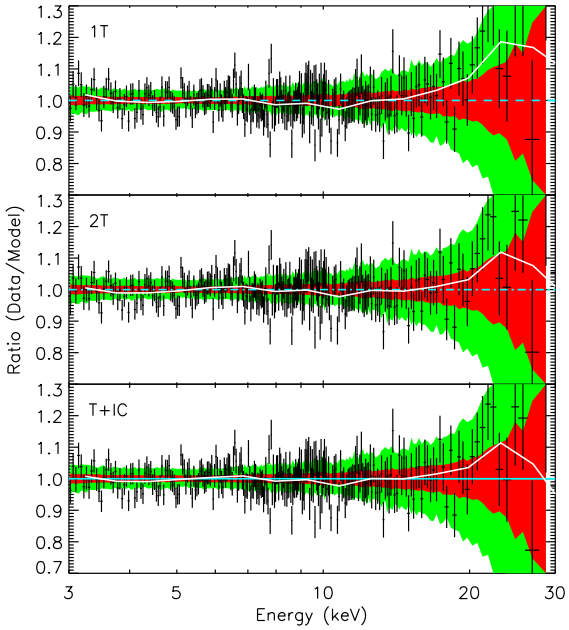

Figure 6. Ratio of the spectrum (crosses, using the nominal background model; all spectra from Figure 4 have been combined for clarity) to each model. The red/dark and green/light shaded regions are the same as in Figure 5. Although difficult to tell, the 2T and T+IC models better describe the overall spectral shape from 3–20 keV, producing flatter residuals than the 1T model; the white line in each plot represents the same data shown as crosses but more heavily binned to accentuate the broader spectral shape relative to the models. The rise from 20–22 keV is likely a background line(s) imperfectly subtracted; note that the feature is within our estimated 3σ uncertainty for the background reconstruction.

(A color version of this figure is available in the online journal.)

the index flattens at lower energies as is seen in, e.g., the Coma cluster (Thierbach et al. 2003). For comparison purposes and for our primary result, we choose to fix $\Gamma = 1.86$, which is similar to the typically assumed value of $\sim$2 in any case.

4.2.2. Fitting the Three Models

Typical fits to the four spectra, using a background spectrum generated from the nominal background model, illustrate the subtle differences between the 1T, 2T, and T+IC descriptions of the Bullet cluster's spectrum in Figures 5 and 6. (Note: all uncertainties quoted in this subsection are purely statistical and are derived using the nominal backgrounds displayed in the above figures.) In each of these figures, the data, backgrounds, and models for the four spectra have been grouped together for clarity, although the models are folded through each response separately during the fit. The background is also shown to highlight where the spectrum becomes dominated by the background. To zeroth order, the 1T fit is quite good, with a typical $\chi^2_{\rm red} \sim 1.01$. The global temperature of $kT \sim 14.2^{+0.3}_{-0.2}$ keV agrees quite well with the acceptable *Chandra* best-fit temperature range of 13.6 keV $\lesssim kT \lesssim$ 14.8 keV (Markevitch et al. 2002), which varies depending on the value of $N_{\rm H}$ used. Although higher than the *XMM-Newton* best-fit global temperature of $\sim 12 \pm 0.5$ keV (Petrosian et al. 2006), we would expect the average temperature in the 3–30 keV band to be slightly higher than measured in the 1–10 keV band. The *Chandra* and *XMM-Newton* temperature disagreement almost certainly comes down to their respective calibrations, e.g., Nevalainen et al. (2010). Despite the somewhat coarse spectral resolution around the Fe lines, the large effective area and exposure time allows the abundance to be well constrained at 0.23 ± 0.03 of solar, consistent with those determined from previous observatories, such as *XMM-Newton* (0.24 ± 0.04, Petrosian et al. 2006).

Although a 1T model can largely explain the detected emission, a very slight curvature in the residuals of the fit indicates that the spectrum is not of a truly isothermal plasma. Because our sensitivity extends up to higher energies, we can test whether that extra curvature is more likely to come from the true multi-temperature structure of the cluster or an IC component. The 2T model approximates what is actually a fairly smooth, somewhat bimodal, temperature distribution (e.g., Andersson et al. 2007), so the best-fit thermal components in this model only roughly correspond to the actual temperatures. Even so, the temperatures we find for the two components are reasonable, with $kT_{\rm high} = 15.3^{+8.4}_{-3.6}$ keV and $kT_{\rm low} = 5.3^{+3.4}_{-3.0}$ keV. Figure 5 shows the relative importance of the fainter component, with the lower temperature accounting for only $\sim$5% of the 3–30 keV flux. The hard spectral tail up to 30 keV is fully consistent with a thermal spectrum of $\sim$15.3 keV, only a little higher than the ambient, non-"bullet" ICM temperature of $\sim$14 keV seen with *Chandra* (Govoni et al. 2004) and the 14.2 keV temperature found here with the 1T model. Given that at a minimum there is recently shocked gas at much higher temperatures (Markevitch 2006), a rise in $kT_{\rm high}$ of this magnitude is not surprising. Also, the range in temperatures for $kT_{\rm low}$ agrees very well with temperatures common in both the "bullet" region and nearby (Andersson et al. 2007).

Finally, we evaluate the likelihood of an IC excess at high energies with the T+IC model. The near success of the 1T

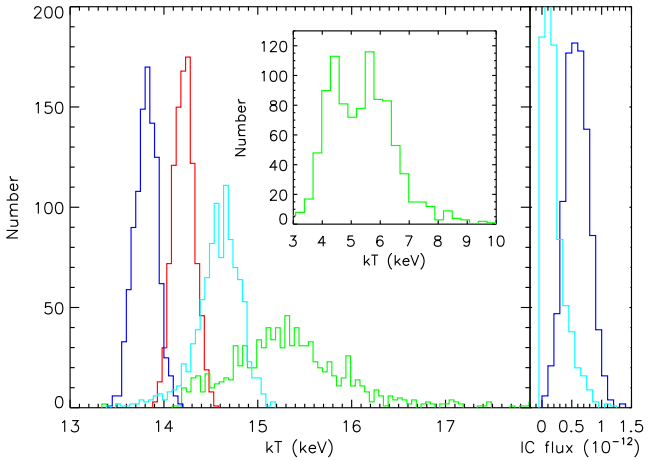

Figure 7. Best-fit temperatures from the 1T (red), 2T (green), T+IC (fixed $\Gamma = 1.86$, blue), and T+IC (free Γ, cyan) models fit to the Bullet cluster spectrum using 1000 realizations of the background that include systematic fluctuations. The background minimally affects the temperature components that depend primarily on high signal-to-noise parts of the spectrum, as in the 1T and T+IC cases, but has a much stronger impact on the 2T components ($kT_{\rm low}$ shown in inset panel while $kT_{\rm high}$ shown in the main panel) which are more sensitive to lower signal-to-noise bins. The right panel shows the distribution of the best-fit power-law fluxes (50–100 keV, units of erg s^{-1} cm^{-2}) for the IC components.

(A color version of this figure is available in the online journal.)

model suggests that if a detectable IC component lies at harder energies, the thermal emission should be well accounted for by a single temperature component. We again find a very reasonable temperature of $kT = 13.8^{+0.5}_{-0.2}$ keV, and the resulting 50–100 keV IC flux is $(0.58 \pm 0.40) \times 10^{-12}$ erg s^{-1} cm^{-2}. Again, the thermal component is entirely consistent with that found with previous observatories. The IC flux, on the other hand, falls nearly a factor of three below the expected value of $(1.58^{+0.43}_{-0.47}) \times 10^{-12}$ erg s^{-1} cm^{-2} (Ajello et al. 2010). Unfortunately, the best-fit IC component only surpasses the thermal component at $\gtrsim$40 keV, where the cluster emission becomes so faint it is lost in statistical fluctuations of the background. To first order, the spectrum appears equally well-fit by the addition of a non-thermal model as by the addition of another thermal model, and the statistical significance of the IC component is possibly high enough to warrant a detection. The inclusion of systematic uncertainties and a detailed comparison of the 2T and T+IC fitting results outlined in the following subsection, however, preclude us from making such a claim.

4.2.3. Relative Performance of Each Model

The mean parameter values and statistical errors were reported in Section 4.2.2; however, true uncertainty ranges must include the impact of both statistical and systematic fluctuations in the background on the fits. The distribution of best-fit temperatures for the three models—found using 1000 realizations of the background for our 4 spectra—are shown in Figure 7, immediately illustrating the impact of both background uncertainties and the model we choose to use on our ability to evaluate the spectrum. When the shape of the model is determined by one parameter, as in the 1T case, background uncertainties have only a slight effect on the temperature, creating a spread of only 0.18 keV (compared to the statistical uncertainty of ∼0.25 keV). Adding another parameter that more finely controls the broad-band shape of the model (2T or T+IC cases) allows background fluctuations to play a more significant role. For the 2T model, the best-fit temperatures for each component—shown in green in the main panel and inset panel of Figure 7—are much more sensitive to background fluctuations than in either the 1T or T+IC cases, mostly owing to the greater flexibility of the model to adjust to small changes in the shape of the spectrum. Background variations primarily affect the $kT_{\rm high}$ component, since a slightly higher/lower background will cause the spectrum to turn over at a lower/higher energy, thus pushing $kT_{\rm high}$ to lower/higher values. The $kT_{\rm low}$ component then adjusts to "correct" the low energy part of the spectrum; the two temperatures are strongly correlated for a given fit, such that a higher than typical $kT_{\rm high}$ will have a higher than typical $kT_{\rm low}$.

In the T+IC model, the temperature component dominates at all relevant energies and thus maintains the precision of the 1T model's temperature (despite having a larger statistical error of 0.35 keV). The IC flux, in principle, should be much more sensitive to background systematics than to statistical uncertainties, for the simple reason that its shape more closely matches the background and any systematic shift up or down of the background will correspondingly shift the IC normalization. Tellingly, the uncertainty due to the background on the IC flux (0.33×10^{-12} erg s^{-1} cm^{-2}, 50–100 keV) is slightly less than its statistical uncertainty (0.4×10^{-12} erg s^{-1} cm^{-2}). A true non-thermal excess at high energies should be more affected by background fluctuations. The IC component dominates at high energies, so it will adjust the most to changes in the background level if it is being driven by the harder emission. Because this is not the case, it is likely driven more by "correcting" (as in the 2T case) the model shape at lower energies, where the signal-to-noise is higher. The IC component is not accounting for truly non-thermal flux in these fits; instead, it substitutes for additional thermal components missing from the single temperature model, likely at both the high *and* low energy ends of the spectrum.

Allowing the IC photon index to be a free parameter further confirms this explanation. For the nominal background, the index steepens to ∼2.4 and mirrors the contribution of the $kT_{\rm low}$ component of the 2T model at low energies, where its continuum shape is nearly identical to that of a ∼5 keV plasma. As shown by the cyan histograms in Figure 7, the temperature of the thermal component in this T+IC model is actually hotter than for the 1T case. The hard emission is modeled entirely by the thermal component, while the IC appears to be mimicking the $kT_{\rm low}$ component. This argument alone does not invalidate the IC hypothesis, since in principle the gas could be sufficiently isothermal to allow IC emission to be contributing excess flux at lower energies where the component is mostly being constrained, and it is only coincidental that the spectrum runs out of counts just when the IC component begins to dominate the hard emission. Assuming this viewpoint, a combination of the statistical and systematic uncertainties gives a most likely IC flux of $0.58 \pm 0.52 \times 10^{-12}$ erg s^{-1} cm^{-2}, or a positive fluctuation of less than 2σ. Considering we have strong reason to believe this component is thermal in nature, it is clear we do not detect IC emission in the global Bullet cluster spectrum with *NuSTAR*. The results for each model, including statistical and systematic uncertainties, are summarized in Table 2.

Even so, the T+IC model may fit the spectrum better than the 2T model, in which case we might still argue that the spectrum shows evidence of an IC component. The relative quality of the T+IC versus 2T fits depends on the background realization being used, and Figure 8 demonstrates that certain backgrounds do in fact favor the T+IC over the 2T model. In this figure, the fits with the 1000 background realizations have been binned

according to the difference in C-statistic values between these two models, with values to the right of the vertical lines favoring the 2T model and values to their left favoring the T+IC model. The solid histogram/vertical line correspond to fits with Γ fixed to a value of 1.86 and the dashed versions to fits with Γ as a free parameter. In the majority of background realizations, the 2T model is preferred, and in only 1.2% of them can the same be said for the T+IC model where Γ is fixed. The T+IC model is favored 7.6% of the time when Γ is free, although in this case the IC component may simply be mimicking a second thermal component. So while it is most likely the case that the spectrum can best be characterized with a pure thermal model, we cannot rule out an IC flux within the range of fluxes in the right panel of Figure 7.

Based on this analysis, a fair 90% upper limit on the IC flux should correctly incorporate both the systematic and statistical uncertainties already discussed. To capture the fact that the T+IC fits prefer a non-zero IC flux, we sum the mean flux with the quadrature-summed uncertainties, yielding an upper limit of 1.1×10^{-12} erg s^{-1} cm^{-2} in the 50–100 keV band.

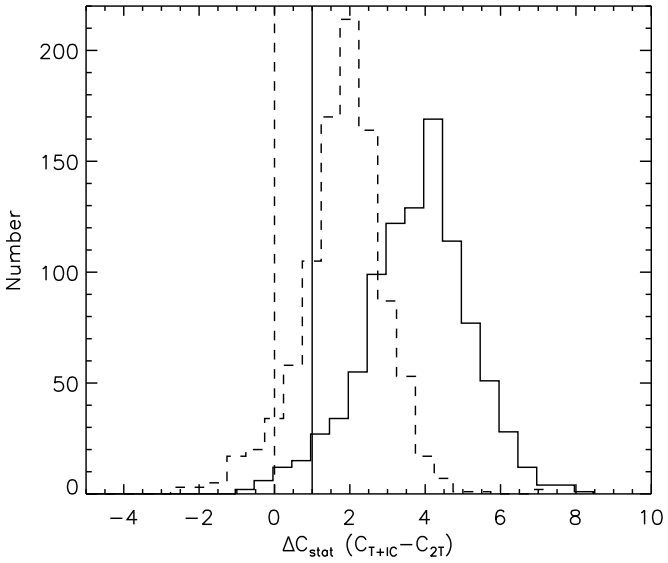

Figure 8. Difference of Cash statistic values between the T+IC and 2T models for each of the 1000 background realizations, which include statistical and systematic fluctuations. The solid and dashed histogram and lines refer to fits where the IC components used a fixed (Γ = 1.86) or free (Γ ∼ 2.4) photon index, respectively. Values to the left of the solid/dashed line show realizations in which the T+IC model is favored, while values to the right have the 2T model favored. The solid line is drawn at ΔC = 1 since the 2T model has one more free parameter than the T+IC model when Γ is fixed. For the majority of background realizations, the 2T model is clearly favored over a spectral model including a non-thermal component.

5. SUMMARY AND DISCUSSION

5.1. Brief Summary

The Bullet cluster was observed by *NuSTAR* in two epochs for a cumulative 266 ks of conservatively cleaned exposure time. The cluster is clearly detected below ∼30 keV with an energy-dependent morphology consistent with the extrapolation of projected temperature maps obtained with *Chandra* and *XMM-Newton*. Above ∼30 keV, potential emission associated with the ICM consists of <10% of the counts per channel. The average temperature of the global spectrum is 14.2 ± 0.3 keV, in good agreement with estimates from *ROSAT*+*ASCA* (14.5 keV, Liang et al. 2000) and *Chandra* (14.8 keV, Markevitch et al. 2002), but somewhat higher than independent estimates from *XMM-Newton* and *RXTE* (∼12 keV, Petrosian et al. 2006). Given the differences between instrument sensitivity and the accuracy of their respective calibrations, we do not suggest any significant discrepancy.

In order to search for a non-thermal excess above the thermal emission at hard energies, we invested a good deal of effort to understand the largest uncertain factor: the background. We constructed an empirical, spatial-spectral model of the background from blank sky data and applied it to our observations to derive a "most likely" model background spectrum for the region containing cluster emission. After evaluating the important systematic uncertainties in the model, 1000 realizations of the background are generated and each subtracted from the spectrum, which is fit with three spectral models representing a simple (1T) or more realistic (2T) thermal-only origin, or a significant IC component at the highest detectable energies (T+IC), for the emission. In over 98% of the fits, the 2T model was statistically favored over the T+IC model, and reasonable values are obtained for both temperatures in the former. We therefore conclude that no significant non-thermal emission has been detected in the *NuSTAR* observations of the Bullet cluster and place an upper limit on the IC flux of

Table 2
Fit Parameters[a]

Model	kT (keV)	Abund. (Rel. to Solar)	Norm.[b] (10^{-2} cm^{-5})	kT or Γ (keV or. . .)	Norm.[b] or IC flux[c] (10^{-2} cm^{-5} or 10^{-12} erg s^{-1} cm^{-2})	C-stat
1T	$14.2^{+0.3,+0.2}_{-0.2,-0.2}$	0.23 ± 0.03, 0.01	1.61 ± 0.02, 0.01	...	...	5717^{+138}_{-138}
2T	$15.3^{+8.4,+2.6}_{-3.6,-0.9}$	0.22 ± 0.04, 0.01	$1.45^{+0.03,+0.12}_{-1.05,-0.32}$	$5.3^{+3.0,+2.4}_{-3.4,-1.8}$	$0.22^{+1.12,+0.56}_{-0.26,-0.12}$	5708^{+137}_{-138}
T+IC	$13.8^{+0.5,+0.2}_{-0.2,-0.2}$	0.24 ± 0.04, 0.01	$1.51^{+0.10,+0.06}_{-0.03,-0.06}$	1.86(fixed)	$0.58^{+0.40,+0.35}_{-0.40,-0.32}$	5713^{+137}_{-141}
T+IC[d]	$14.6^{+0.4,+0.3}_{-0.4,-0.5}$	0.26 ± 0.05, 0.02	$1.49^{+0.1,+0.06}_{-0.1,-0.07}$	$2.4^{e,+0.4}_{-1.3,-0.4}$	$0.12^{+0.06,+0.44}_{-0.06,-0.09}$	5710^{+136}_{-140}

Notes.
[a] Uncertainties are 90% statistical and due to background systematics, respectively.
[b] Normalization of the MeKaL thermal spectrum, which is given by $\{10^{-14}/[4\pi(1+z)^2 D_A^2]\} \int n_e n_H \, dV$, where z is the redshift, D_A is the angular diameter distance, n_e is the electron density, n_H is the ionized hydrogen density, and V is the volume of the cluster.
[c] 50–100 keV.
[d] Statistical errors on flux computed with Γ fixed at 2.4 while the systematic errors give the range of fluxes for each best-fit Γ and normalization.
[e] Upper bound on the statistical uncertainty unconstrained.

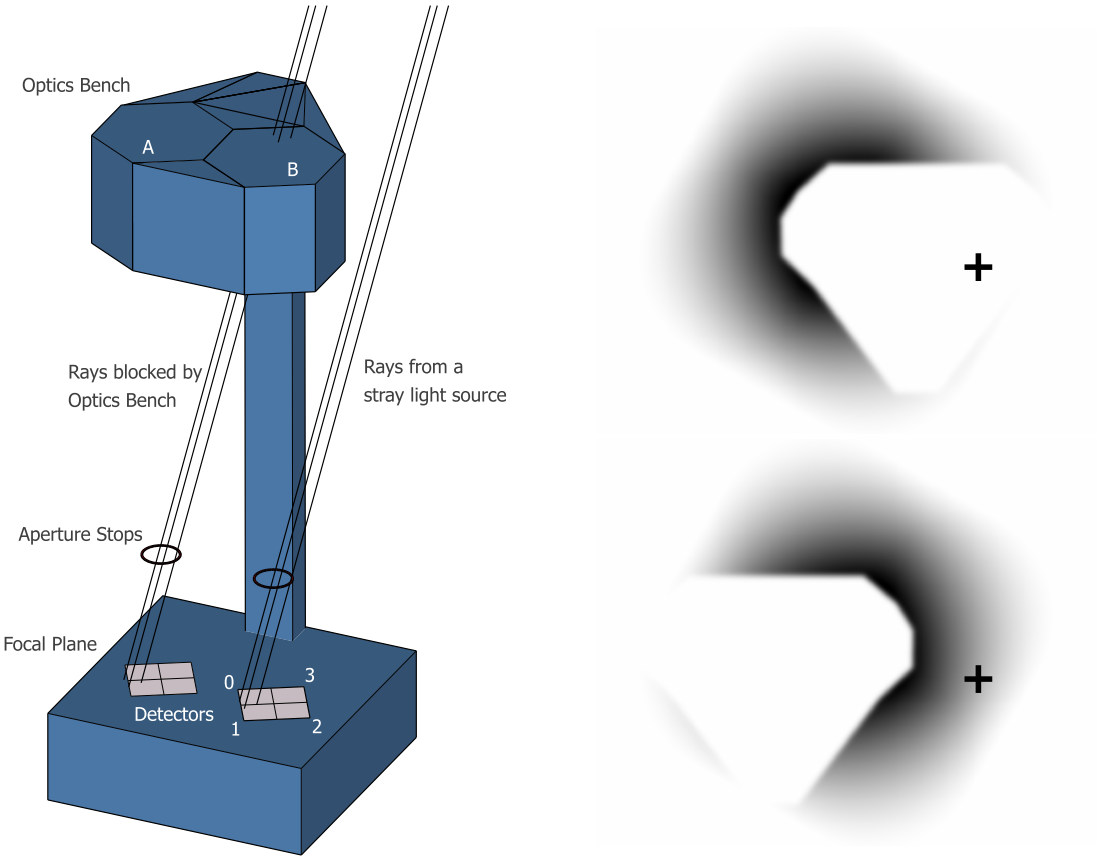

Figure 9. Left: a schematic of the observatory that illustrates how far off-axis sources can directly shine on the detectors through the aperture stop, producing the "Aperture" background. In this example, rays from the source are shielded from striking the left (A) detector plane by the optics bench, but other rays from the same source have an unimpeded path through the aperture stop to shine on a corner of the right (B) detector plane. Right: the location of sources on the sky, as visible from the detector plane, that produce the "Aperture" background for telescopes A (top) and B (bottom). The images are weighted (darker) by the number of detector pixels a given source shines on. The crosses give the approximate position of the source shown in the left panel.

(A color version of this figure is available in the online journal.)

1.1×10^{-12} erg s^{-1} cm^{-2} (50–100 keV). This flux falls below that reported by *RXTE* and *Swift*.

5.2. Comparison to and Implications Regarding Previous Results

As mentioned in Section 1, Petrosian et al. (2006) first suggested the existence of significant IC emission at hard energies in the Bullet cluster based on a joint analysis of *XMM-Newton* and *RXTE* spectra. The uncertainty in the measurement of $(3.1 \pm 1.9) \times 10^{-12}$ erg s^{-1} cm^{-2} (50–100 keV) is too large to justify a claim of detection. However, a more recent analysis (Ajello et al. 2010) using a *Swift* BAT spectrum found a flux of $(1.6 \pm 0.5) \times 10^{-12}$ erg s^{-1} cm^{-2} (50–100 keV), roughly consistent with that from Petrosian et al. (2006). Both fluxes are only barely in conflict with our conservative upper limit, but our most likely IC flux of $(0.58 \pm 0.52) \times 10^{-12}$ erg s^{-1} cm^{-2} (50–100 keV) is clearly inconsistent with these previous measurements (all above uncertainties are given at the 90% confidence level)

The origin of the discrepancy has two potential explanations: either the spectra from the various instruments disagree; or the approach to modeling the spectra disagree. While even minor calibration differences between the characterization of the telescope responses and of the backgrounds can significantly affect results, a comparison of the *RXTE*, *Swift*, and *NuSTAR* spectra fit to 1T or 2T models implies these are not responsible. None of the instruments on these satellites reliably detect emission above 30 keV from the Bullet, and below this energy there is no compelling excess above a reasonable thermal-only model in Figure 2 of Petrosian et al. (2006), the lower left panel of Figure 5 of Ajello et al. (2010), or Figure 5 of this paper. At higher energies, the background dominates the count rate and its treatment becomes crucial, where even small fluctuations can result in a false IC signal. It is beyond the scope of this paper to evaluate the backgrounds from the other two missions, but no causes for worry are evident in the analyses of the *RXTE* and *Swift* data.

If the spectra are all consistent with each other, we must attribute the conflicting conclusions to differences in how the spectra are modeled. In principle, there should be no difference, since 1T, 2T, and T+IC models are each tried in all three analyses. The crucial distinction between them is the minimum energy used in the fits: 1 keV (Petrosian et al. 2006), 0.5 keV (Ajello et al. 2010), or 3 keV (this work). The lower end of the energy range matters because the thermal gas of the Bullet cluster is decidedly *not* isothermal (Markevitch et al. 2002), and the fraction of the emission any temperature component contributes strongly varies with energy, with low temperature components dominating at soft energies but essentially disappearing from the hard band. Merging clusters, especially those like the Bullet where one subcluster

hosts a cool core, may have components of roughly equal emission measure that span a factor of two in temperature. In particular, the emission coming from the cool core ranges from $kT \lesssim 4$ keV up to 7 keV, has a higher abundance, and mostly contributes at the lowest energies. The gas associated with the main subcluster is hotter, with a central $kT \sim 12$ keV and shocked regions to the W and also to the slight SE with $kT \gtrsim 16$ keV (M. Markevitch 2013, private communication). Given the extreme range in temperatures, even a 2T model may provide an insufficient description of the data over a broad energy range. Ironically, the T + IC model might better fit the *purely thermal* emission more successfully in this case, since a power law with free photon index is able to simultaneously account for emission from components at either extreme of the temperature distribution (e.g., A3112, Bonamente et al. 2007; Lehto et al. 2010).

By including data below 3 keV in order to better constrain the thermal component, in all likelihood the larger consequence is to bias the characterization of the thermal component, since only simple spectral models are considered. Because the response of *XMM-Newton*'s EPIC instruments peaks between 1–2 keV and shot noise, which has a fractional error decreasing with energy, sets the signal-to-noise ratio, fit minimization routines are overly biased to find good fits at these lower energies. The second model in the multi-component fits of Ajello et al. (2010), from this perspective, are focused on artificially "fixing" the residuals below 1 or 2 keV with either the second temperature or IC component, and the slope of the IC's photon index is determined mostly by the *XMM-Newton* data alone, given that the T + IC model overpredicts almost every BAT data point. This explanation is less compelling for the *XMM-Newton* + *RXTE* analysis of Petrosian et al. (2006). In this case, the fact that fits to both the *XMM-Newton* (over 1–10 keV) and *RXTE* (over 3–30 keV) yield the same temperature despite the different energy bands is worrisome; given the multi-temperature structure, one would expect the 3–10 keV temperature from *XMM-Newton* to be hotter than this average, and the 3–10 keV temperature from *RXTE* to be cooler or unchanged.

In contrast, the temperatures in our 2T model roughly agree with the approximately bimodal temperature distribution seen with *Chandra*, lending credence to the still imperfect thermal model approximated with only two components. The much improved spectral resolution of *NuSTAR* over that of *RXTE* and *Swift* undoubtedly helps the fit find physical temperatures. For the T + IC model, when the photon index is left free, it tends toward a somewhat larger or steeper value where it only influences the lowest energy channels. The IC component, when exhibiting this behavior, mimics a lower temperature thermal component more than it tries to account for any excess emission at high energies, further refuting the existence of a significant non-thermal excess.

By combining the synchrotron spectrum at radio frequencies with an IC estimate or upper limit, we can directly constrain the volume averaged magnetic field strength. Following the arguments and expression for B in Equation (14) of Wik et al. (2009), we use the total radio halo flux of 78 mJy at 1300 MHz and a radio spectral index of 1.2–1.4 (Liang et al. 2000). The radio spectrum exhibits no flattening at lower frequencies as in Thierbach et al. (2003) for the Coma cluster, so we assume the spectrum continues as a power law to lower frequencies where the electron population producing the synchrotron is the same as those producing the IC. The upper limit on IC emission translates to a lower limit on the magnetic field strength of $B \gtrsim 0.2$ μG, which is comparable to values found in other clusters using *Suzaku* and *Swift* data (e.g., Ota et al. 2014; Wik et al. 2012). Unlike estimates of $B \sim 0.1$–0.2 μG, such lower limits are more consistent with equipartition estimates ($\sim$1 μG for the Bullet cluster, Petrosian et al. 2006) and Faraday rotation measure estimates in other clusters, which typically place the field strength at a few μG (e.g., Kim et al. 1990; Clarke et al. 2001; Bonafede et al. 2010). While it is possible to reconcile these estimates with a lower volume averaged value of B, our lower limit does not requires it.

5.3. Implications for Future IC Searches

In order to detect diffuse, faint IC emission in galaxy clusters, the IC signal must be teased from both thermal and instrumental "backgrounds," both of which are likely to be brighter than the IC emission itself. While going to harder energies reduces contaminating emission from the thermal gas, it requires a large effective area at high energies and/or low and well-characterized instrumental and/or cosmic backgrounds. Regarding the background, focusing optics like those on board *NuSTAR* have clear advantages over non-focusing ones, such as collimators and coded-mask telescopes. The effective area or equivalent sensitivity, however, remains a greater challenge for reflective optics due to the large number—and thus weight—of mirror shells needed. IC photon intensity also declines rapidly with energy, making it exceedingly difficult to detect such emission at high energies given the statistical fluctuations of a realistic background level without a very large effective area. In the foreseeable future, IC emission in hot clusters will only be detectable as a subtle inflection of the thermal tail. Such non-thermal inflections, however, are complicated by having plausible alternative origins, such as background AGNs, clumps of super hot gas, and slightly underestimated overall backgrounds. These difficulties, combined with magnetic field equipartition estimates nearly an order of magnitude larger than the field strengths inferred by IC measurements, emphasize the need for a conservative approach.

The recent history of IC searches seems to justify this view. Ota et al. (2014) nicely summarizes some *RXTE*, *Beppo-SAX*, *Swift*, and *Suzaku* detections and upper limits in their Figure 10, which shows that clusters may exhibit an IC signal in the data set of one observatory but not another—sometimes, but not often, contradictorily. The reasons behind these differences are not always clear, but likely include some combination of relative instrumental calibration, background treatment, and telescope capabilities. Detections are only mildly statistically significant and are in danger of being compromised by the complications mentioned above. The clusters expected to host IC-producing electrons are those undergoing mergers, which produce—possibly extreme—multi-temperature distributions. Such distributions should in principle be straightforward to separate from a non-thermal component, *if* the IC component begins to dominate the spectrum at an energy where the signal-to-noise is sufficiently high, including systematic uncertainties. For the Bullet cluster, we reach this point around 20–30 keV.

The next mission capable of detecting IC emission associated with radio halos is *Astro-H*, which will include a Hard X-ray Telescope (HXT) and Imager (HXI), with a sensitivity comparable to *NuSTAR*, as well as substantial soft X-ray capabilities with the Soft X-ray Imager (SXI) and Soft X-ray Spectrometer (SXS). Although the HXI alone provides for some improvement over *NuSTAR*, the SXI and especially the SXS

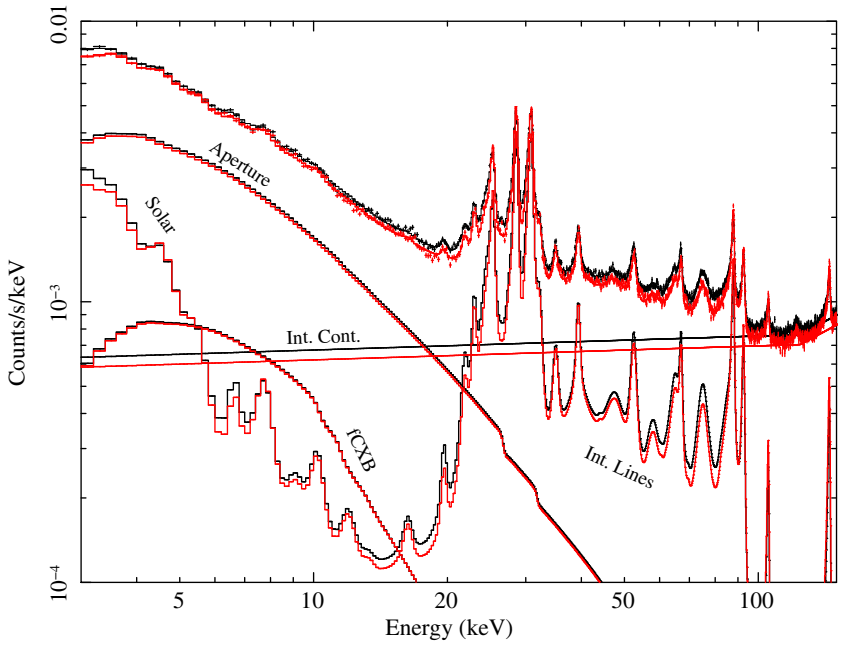

Figure 10. Initial independent fits to stacked blank sky data for telescopes A (black) and B (gray or red). The spectra for each of the four detectors in each focal plane are averaged together when combined, such that the rates shown are also per detector. The major contributions are labeled according to their source with the "Aperture" or $A_d(E, x, y)$, "fCXB" or $f_d(E, x, y)$, and "Solar" or $S_d(E)$ components having a cosmic origin and the "Int. Cont." and "Int. Lines" components, together making up the $I_d(E)$ term, having an "internal" or instrumental origin largely the result of the spacecraft environment. Because the spectral shapes are identical, the "Aperture" component consists of both emission directly from the CXB through the aperture stop and from CXB emission reflected/scattered off the backside of the aperture stop and/or other parts of the telescope.

(A color version of this figure is available in the online journal.)

should allow for a more detailed and complete accounting of the thermal components of target clusters through emission line diagnostics. A better understanding of the thermal continuum will make marginal non-thermal-like excesses at hard energies more significant and upper limits more constraining.

If the average magnetic field strength in galaxy clusters hosting radio halos is typically closer to $\sim$1 μG than the $\sim$0.2 μG implied by past detections, even *Astro-H* is unlikely to be enough of a technical advance. Because the ratio of synchrotron to IC flux scales with the energy density of the of the magnetic field ($\propto B^2$), a 5$\times$ stronger B requires a 25$\times$ more sensitive telescope than currently exists. IC emission at this level would only compete with the thermal emission of a Bullet-like cluster between 30–50 keV, and given how faint the cluster is at these energies relative to the background (e.g., Figures 5 and 16), it is likely that most of the sensitivity gain will come from increasing the effective area. An increase in effective area over *NuSTAR* of not quite an order of magnitude would be achieved by the proposed probe class *HEX-P* mission,[12] so a substantial decrease in background and its systematic uncertainty would still be necessary.

In terms of past IC detections, it may be the case that what has been measured is not IC emission associated with large-scale radio halos. Instead of being associated with the electrons producing radio halos and relics, the IC emission might originate from electrons accelerated by accretion shocks at the virial radius (e.g., Kushnir & Waxman 2010; Keshet et al. 2012). Non-imaging telescopes—unlike *NuSTAR*—would pick up this emission, which peaks in surface brightness $\gtrsim$Mpc from cluster centers. Given our restricted extraction region around the Bullet cluster, we are not sensitive to these electrons. However, the FOV does partially include the virial region, where we characterized the background, so in principle this IC emission could exist at very faint levels; a cursory check for a non-thermal component was made when the background was fit, but no such signal beyond the generic background model was apparent. Note that these observations are not ideally suited for searches of this emission, which would be better served by several offset pointings around the periphery of the cluster. Even so, the emission would be strongest at the low energy end, where we attribute extra flux detected in the background regions to scattered thermal photons. It should be feasible to constrain these models, but only after a more detailed accounting of the Bullet cluster's thermal structure has been undertaken, in order to separate local emission from scattered photons from various regions in the cluster. We will address this issue in a future paper focused on the hard X-ray weighted temperature structure, including extreme temperature shock regions.

This research was supported by an appointment to the NASA Postdoctoral Program at the Goddard Space Flight Center, administered by Oak Ridge Associated Universities through a contract with the National Aeronautics and Space Administration (NASA) and made use of data from the *NuSTAR* mission, a project led by the California Institute of Technology, managed by the Jet Propulsion Laboratory, and funded by NASA. We thank the *NuSTAR* Operations, Software, and Calibration teams for support with the execution and analysis of these observations. This research has made use of the *NuSTAR* Data Analysis Software (NuSTARDAS) jointly developed by the ASI Science Data Center (ASDC, Italy) and the California Institute of Technology (USA). The authors wish to thank Maxim Markevitch for providing a 0.5 Ms *Chandra* image of the Bullet cluster to

[12] http://pcos.gsfc.nasa.gov/studies/rfi/Harrison-Fiona-RFI.pdf

confirm the cluster region lacks bright point sources and the referee for helpful comments that improved the paper.

APPENDIX A

DEFINITION OF THE BACKGROUND MODEL

A.1. Overview

The *NuSTAR* observatory design gives rise to various, independent background components that vary spatially across the FOV, complicating standard background estimation techniques. The purpose of this Appendix A is to describe in detail the terms of Equation (1) and how they were derived. By completely describing the background as a function of pixel position x, y and energy E, otherwise empty regions can be employed to accurately estimate the background inside the region containing a source of interest. The features of $B_d(E, x, y)$ are constrained by stacked "blank" field observations, taken from the deep (ECDFS) and medium (COSMOS) survey data, listed in Table 3.

NuSTAR consists of two separate telescopes (two sets of optics, housed in the optics module, focusing onto two focal planes, housed in the focal plane module). The telescopes and associated data/response functions are referred to as A and B. Each focal plane consists of a 2×2 array of CdZnTe detectors with a 32×32 array of pixels. In principle, each pixel has a unique background response, but in practice all the pixels on a single detector—excepting edge pixels—behave comparably. Due to differences in thickness and other properties of the detectors, the instrumental background $I_d(E)$ for each detector is unique, but largely similar. The low altitude and inclination orbit of *NuSTAR* minimizes SAA activation and proton flares, so the instrumental background dominating at higher energies is low and stable.

The benches containing the optics and detectors are separated on two ends of an unenclosed mast. Pointing variations throughout a given observation cause a given detector pixel to sample several times more sky than without this wobble. Because the light path is open to space, stray light from the CXB is able to skirt between the optics bench and the aperture stops in front of the two focal planes (Figure 9); the geometry of this window produces highly non-uniform background gradients across the detectors, captured by the $A_d(E, x, y)$ term and called the "Aperture" background. At the lowest energies, scattered "Solar" X-rays $S_d(E)$ reflected from other parts of the observatory structure are visible to the detectors, due to its open design. Typically, the least significant component is the focused cosmic background $f_d(E, x, y)$, made up of extragalactic and/or Galactic point source and diffuse emission, such as the Galactic Ridge X-ray emission. Here we ignore Galactic contributions and focus on the components relevant to observations at high Galactic latitude.

The spectral components, fit to a stacked spectrum of the observations from Table 3 for the entire FOV, are shown in Figure 10. The "Solar" $S_d(E)$ component is shown with part of the instrumental $I_d(E)$ component, due to their identical implementation in `XSpec`, and $I_d(E)$ is decomposed into continuum and line components for similar reasons.

Below ~20 keV, the background is dominated by the "Aperture" background. Below ~5 keV, the steep "Solar" component increases the background and is most likely due to reflected solar X-rays as evidenced by its persistence in spectra from Earth observations when the satellite is illuminated by the Sun and its absence when not. This component can undergo significant fluctuations due to solar activity. Although thought to come primarily from reflections off the backside of the aperture stop, this conjecture has yet to be confirmed and thus we have no way to predict the spatial pattern it produces on the detectors, but it is likely non-uniform as well. The other low energy contributor to the background—the "fCXB"—includes both truly focused events (photons reflected off of both mirrors) and scattered events or ghost rays (photons reflecting off of only one mirror) from the many unresolved sources both within and outside the FOV. Its shape is roughly flat across the detector plane despite vignetting due to an increase in scattered light from sources outside the FOV at larger off-axis angles. However, cosmic variance can add strong spatial variations within and between fields.

Above ~15–20 keV, the internal or instrumental background dominates. It is made up of gamma rays Compton scattered by the detector and shield, lines activated by interactions between the spacecraft/detectors and the radiation environment in orbit, and a few fluorescence lines. Most of the lines are driven by frequent—if glancing—passages through the SAA, when protons activate material in the focal plane module near or in the detectors. Unstable elements are created by proton spallation and secondary neutron capture by cadmium, which then radioactively decay with half-lives typically longer than *NuSTAR*'s orbital period. The strongest of these activation lines appear in the complex from 22–25 keV. While the strengths of these lines depend on the spacecraft's recent orbital history, there is as yet no evidence for spatial variations across individual detectors, and the relative strength of a given line between detectors—which depends on properties unique to each detector such as its thickness—does not vary. The strongest instrumental lines are due to K-shell fluorescence of Cesium and Iodine at 28 keV and 31 keV, respectively, residing in the anti-coincidence shield.

The continuum, meant to represent the Compton scattered component and any other featureless instrumental components, is modeled as a broken power law with a break at 124 keV. The lines and line complexes are modeled with 29 Lorentzian-profile lines, *empirically* added to the spectra in Figure 10 until the fit can no longer be reasonably improved. Initially, the line energies and widths, which are tied between the A and B spectra, are allowed some freedom during the fitting process—as is the temperature describing the "Solar" component and the indices of the internal continuum—but at some arbitrary point the model is designed to be "good enough" and those parameters fixed thereafter. The internal (and perhaps "Solar") components exhibit no detectable spatial variation within individual detectors, but they do between detectors.

A.2. Spatial Distribution of the "Aperture" Background

To first order, the CXB has a constant surface brightness across the sky, so the intensity detected by a given pixel depends solely on the solid angle Ω of visible sky. The total area of the sky sampled by at least one pixel covers $\Omega = 37.2$ deg^2, of which an individual pixel is exposed to $\Omega \sim 12$ deg^2 of sky as defined by the circular aperture stop. The view is blocked, however, by the apparent position of the optics bench, which depends on the location of the pixel in the focal plane, so the level of CXB flux smoothly varies across the detectors in the range 0.3 deg^2 $< \Omega <$ 10 deg^2. Despite understanding this geometry, the absolute position of the focal plane detectors in the bench is uncertain at the 1 mm level. Also, just as for the "Solar"

Table 3
Observations Used as Blank Sky Fields

Identifier	ObsID	R.A. (J2000)	Decl. (J2000)	Exposure Time (ks)
60022001_ECDFS_MOS001	60022001002	52.9098	−27.9801	41.2
60022002_ECDFS_MOS002	60022002001	53.0333	−27.9783	43.1
60022003_ECDFS_MOS003	60022003001	53.1606	−27.9773	43.2
60022004_ECDFS_MOS004	60022004001	53.2880	−27.9776	43.7
60022005_ECDFS_MOS005	60022005001	52.9167	−27.8658	42.3
60022006_ECDFS_MOS006	60022006001	53.0437	−27.8670	41.6
60022007_ECDFS_MOS007	60022007002	53.1709	−27.8652	44.3
60022008_ECDFS_MOS008	60022008001	53.2943	−27.8599	43.2
60022009_ECDFS_MOS009	60022009001	52.9200	−27.7525	41.7
60022010_ECDFS_MOS010	60022010001	53.0447	−27.7503	42.7
60022011_ECDFS_MOS011	60022011001	53.1693	−27.7543	43.4
60022012_ECDFS_MOS012	60022012001	53.2940	−27.7451	43.9
60022013_ECDFS_MOS013	60022013001	52.9223	−27.6429	44.6
60022014_ECDFS_MOS014	60022014001	53.0487	−27.6448	44.8
60022015_ECDFS_MOS015	60022015001	53.1726	−27.6470	45.1
60022016_ECDFS_MOS016	60022016001	53.2976	−27.6456	42.1
60022001_ECDFS_MOS001	60022001003	52.9234	−27.9547	40.9
60022002_ECDFS_MOS002	60022002002	53.0491	−27.9557	41.2
60022003_ECDFS_MOS003	60022003002	53.1791	−27.9534	41.0
60022004_ECDFS_MOS004	60022004002	53.3070	−27.9520	41.2
60022005_ECDFS_MOS005	60022005002	52.9339	−27.8406	41.2
60022006_ECDFS_MOS006	60022006002	53.0603	−27.8391	41.3
60022007_ECDFS_MOS007	60022007003	53.1772	−27.8472	41.7
60022008_ECDFS_MOS008	60022008002	53.3007	−27.8479	41.8
60022009_ECDFS_MOS009	60022009003	52.9283	−27.7391	41.6
60022010_ECDFS_MOS010	60022010002	53.0527	−27.7335	27.9
60022010_ECDFS_MOS010	60022010004	53.0578	−27.7336	13.2
60022011_ECDFS_MOS011	60022011002	53.1750	−27.7384	41.6
60022012_ECDFS_MOS012	60022012002	53.3002	−27.7373	41.9
60022013_ECDFS_MOS013	60022013002	52.9275	−27.6257	41.6
60022014_ECDFS_MOS014	60022014002	53.0507	−27.6261	44.1
60022015_ECDFS_MOS015	60022015003	53.1795	−27.6221	43.5
60022016_ECDFS_MOS016	60022016003	53.3009	−27.6223	43.9
60021001_COSMOS_MOS001	60021001002	149.7494	2.4728	18.8
60021002_COSMOS_MOS002	60021002001	149.7382	2.3619	22.6
60021003_COSMOS_MOS003	60021003001	149.7280	2.2571	20.5
60021004_COSMOS_MOS004	60021004001	149.7247	2.1449	21.8
60021005_COSMOS_MOS005	60021005001	149.7154	2.0409	21.5
60021006_COSMOS_MOS006	60021006001	149.7090	1.9316	21.7
60021007_COSMOS_MOS007	60021007001	149.8583	2.4636	22.9
60021008_COSMOS_MOS008	60021008001	149.8516	2.3533	23.3
60021009_COSMOS_MOS009	60021009002	149.8459	2.2520	22.8
60021010_COSMOS_MOS010	60021010001	149.8325	2.1400	24.4
60021011_COSMOS_MOS011	60021011001	149.8226	2.0343	25.9
60021012_COSMOS_MOS012	60021012001	149.8138	1.9236	23.0
60021013_COSMOS_MOS013	60021013001	149.9671	2.4582	25.3
60021014_COSMOS_MOS014	60021014001	149.9551	2.3495	22.7
60021015_COSMOS_MOS015	60021015001	149.9484	2.2444	23.4
60021016_COSMOS_MOS016	60021016001	149.9391	2.1344	25.5
60021017_COSMOS_MOS017	60021017001	149.9297	2.0290	22.9
60021018_COSMOS_MOS018	60021018001	149.9212	1.9178	24.0
60021019_COSMOS_MOS019	60021019001	150.0735	2.4506	28.9
60021020_COSMOS_MOS020	60021020002	150.0660	2.3421	28.0
60021021_COSMOS_MOS021	60021021001	150.0538	2.2375	27.4
60021022_COSMOS_MOS022	60021022001	150.0496	2.1231	22.0
60021023_COSMOS_MOS023	60021023001	150.0366	2.0193	24.6
60021024_COSMOS_MOS024	60021024001	150.0288	1.9088	25.4
60021025_COSMOS_MOS025	60021025001	150.1868	2.4395	22.1
60021026_COSMOS_MOS026	60021026001	150.1821	2.3253	28.9
60021027_COSMOS_MOS027	60021027002	150.1707	2.2181	23.9
60021028_COSMOS_MOS028	60021028001	150.1608	2.1086	22.9
60021029_COSMOS_MOS029	60021029001	150.1525	2.0020	22.9
60021030_COSMOS_MOS030	60021030001	150.1439	1.8899	24.0
60021031_COSMOS_MOS031	60021031001	150.2879	2.4247	22.2
60021032_COSMOS_MOS032	60021032001	150.2848	2.3121	25.8

Table 3
(Continued)

Identifier	ObsID	R.A. (J2000)	Decl. (J2000)	Exposure Time (ks)
60021033_COSMOS_MOS033	60021033001	150.2751	2.2075	21.7
60021034_COSMOS_MOS034	60021034001	150.2677	2.0978	19.4
60021034_COSMOS_MOS034	60021034003	150.2641	2.0982	9.4
60021035_COSMOS_MOS035	60021035002	150.2854	2.0520	21.4
60021036_COSMOS_MOS036	60021036002	150.2761	1.9422	22.7
60021037_COSMOS_MOS037	60021037002	150.2650	1.8359	24.1
60021038_COSMOS_MOS038	60021038001	150.3716	1.8270	23.1
60021039_COSMOS_MOS039	60021039001	150.3785	1.9347	22.3
60021040_COSMOS_MOS040	60021040001	150.3850	2.0510	23.8
60021041_COSMOS_MOS041	60021041001	150.3912	2.1512	22.2
60021042_COSMOS_MOS042	60021042002	150.4002	2.2594	22.4
60021043_COSMOS_MOS043	60021043001	150.4036	2.3641	23.8
60021044_COSMOS_MOS044	60021044002	150.4158	2.4753	21.7
60021046_COSMOS_MOS046	60021046002	150.5307	2.5761	17.6
60021046_COSMOS_MOS046	60021046004	150.5329	2.5763	13.0
60021047_COSMOS_MOS047	60021047002	150.5311	2.4709	24.9
60021048_COSMOS_MOS048	60021048002	150.5109	2.3584	24.9
60021049_COSMOS_MOS049	60021049002	150.5062	2.2535	24.7
60021053_COSMOS_MOS053	60021053002	150.4658	1.8190	11.4
60021053_COSMOS_MOS053	60021053004	150.4601	1.8194	5.7
60021053_COSMOS_MOS053	60021053006	150.4660	1.8194	6.2

component, CXB emission from the entire rear hemisphere of the sky—except that blocked by the Earth—can be scattered by the backside of the aperture stop and other parts of the observatory into the focal plane, thus modulating its spatial distribution. Using CXB focal plane maps generated by ray traces through the observatory's geometry, we can adjust the precise position of the detectors within the focal plane and the proportion of unmodulated, scattered CXB flux until we obtain a good match to stacked images of the blank sky observations.

To isolate the "Aperture" component, we stack 7–15 keV images from all the observations in detector (DET1) coordinates, which has a finer spatial resolution than the native pixels (possible due to probability distribution functions relating to event grades obtained from pencil-beam ground calibrations); the stacked images are shown in the left panels of Figure 11. The 40 × 40 mm detector plane is binned into cells with sides 2–4 mm long and fit to the ray trace model using the χ^2 statistic and minimization package `MPFIT` (Markwardt 2009). The ray-trace-based, non-analytic function $A_d(x, y)$ is fit to the images with offsets in the x and y directions and overall normalizations as free parameters. Simultaneously, the I_d, S_d, and f_d terms are included with fixed relative normalizations between detectors, such that $I_1 = c_1 \times I_0$, $I_2 = c_2 \times I_0$, etc., with the constant terms c_d estimated from fits to single detector spectra. The normalizations of the $A_d(x, y)$ terms for telescopes A and B are inconsistent with the expectation from Figure 10 if they only include direct emission through the aperture stop. To reconcile the spatial and spectral "Aperture" models, the spatial model requires additional, spatially flat emission of uncertain origin. One possibility is that Earth albedo or CXB photons are scattered off of the backside of the aperture stop and elsewhere and into the detector housing. Spectra extracted during Earth-occulted periods, for example, exhibit a component below 15 keV with the same spectral shape as the "Aperture" component, even though the CXB is not directly visible (see Figure 12). Alternatively, a contributor to the internal continuum component may rise with decreasing energy instead of following the simple power-law spectrum we assume. The spectral shape of this component is hard to predict, and we make no attempt to do so, but such a rise is very plausible and would likely be spatially flat. For simplicity, the spatial model of the "Aperture" component is modified to include this extra emission, rather than adjusting the spectral shape of internal continuum. The amount of extra emission added is increased until we achieve self-consistency between spectral and spatial fits to the data without large x and y offsets in the $A_d(x, y)$ terms. We also performed simultaneous spectro-spatial fits of similarly binned regions, and while they are the most comprehensive, they are too computationally intensive and fickle to arrive at best-fit offsets and extra "Aperture" emission. However, these fits were useful to explore the parameter space, as were fits to the full FOV spectra, informing the level to which each component should contribute to the 7–15 keV images. This iterative procedure results in extra "Aperture" fractions of 13% for each focal plane and position offsets of (−3.4, 2.0) and (−3.5, 1.6) in (x, y) for A and B, respectively. These exact values are irrelevant as long as the "Aperture" shape is correct; they only matter if one wants to extract an absolute flux for the CXB using this data. The model created with these values is shown in the right panels of Figure 11.

A.3. Determining the Complete Background Model

Because the origin of the "Aperture" component of the background is well understood, we were able to characterize its variation across the FOV with high confidence. The spatial distribution of the two other cosmic sources—"fCXB" and "Solar"—of the background have yet to be as well-constrained. Although the typical "fCXB" distribution can in principle be simulated assuming it is diffuse and uniform, at the time of this writing the model of the mirror modules is still being refined to account for observed ghost ray patterns. (Ghost rays are photons typically scattered by the optics, usually once-reflected, from sources within ∼1° of the optical axis.) The pre-launch

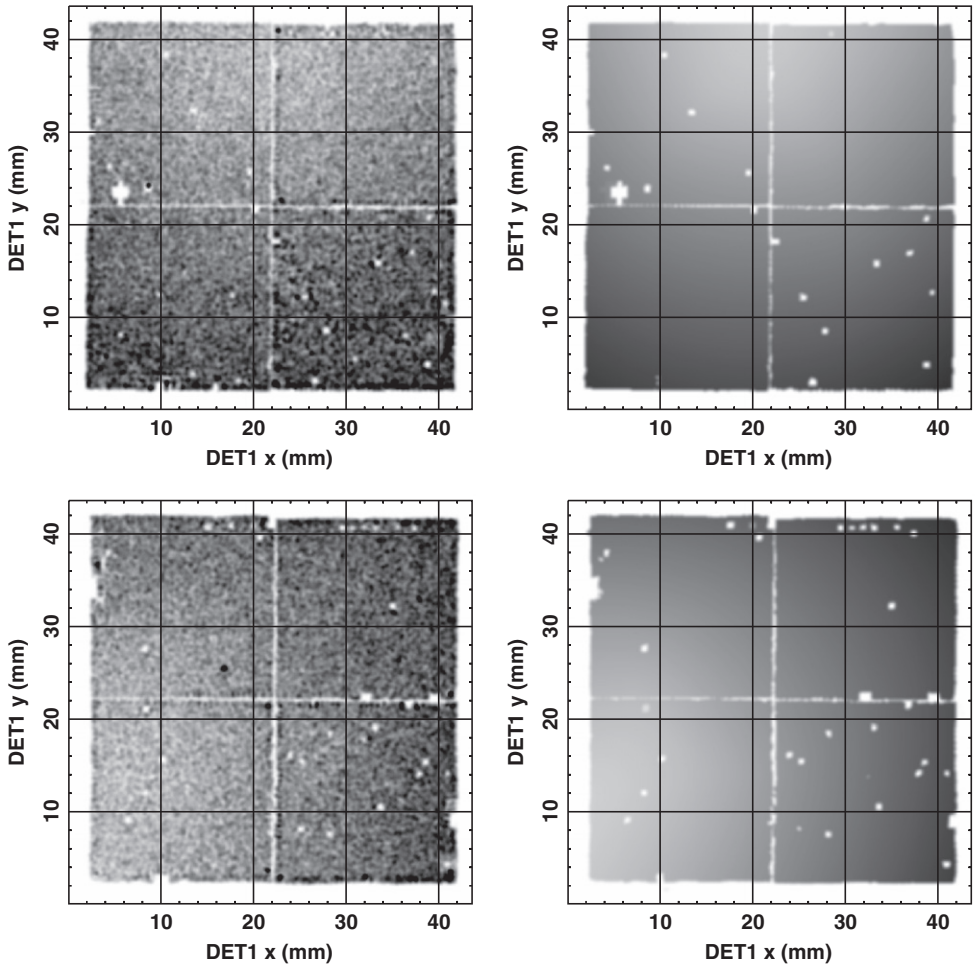

Figure 11. Stacked images in the 7–15 keV band for the blank sky fields (left panels) compared to the best-fit model of the spatial distribution of the "Aperture" background (right panels) for telescopes A (top panels) and B (bottom panels). The data include other background components not included in the model, although they are subdominant in this energy band. Excluded RAW (native) pixels display as white, and detectors 0–3 are arranged counterclockwise with detector 0 in the top right of the focal planes. The gradient spans a linear scale from 0 to 4 counts (white to black), and the data have been smoothed by a Gaussian kernel of width 3 pixels for clarity.

model predicts a distribution somewhat following the vignetting function; however, the blank sky fields show no evidence of such a spatial modulation. Observed ghost ray patterns produced by bright sources near to but outside the FOV show an additional halo farthest from the source, likely due to reflections off the back sides of the mirrors. The extra contribution due to this halo from CXB sources outside the FOV may act to compensate for the drop in flux from higher off-axis sources within the FOV. Empirically, the spatial shape of the "fCXB" is consistent with a flat distribution, although due to its relative faintness it is difficult to discern otherwise. We assume a flat distribution hereafter for simplicity, which is feasible because we are fitting stacked spectra from many fields, so variations due to cosmic variations are reduced.

The "Solar" component has only recently been recognized as originating from the Sun through reflections off the observatory structure. No study of its likely spatial distribution has been undertaken, and in any case the distribution may vary with Sun angle. To allow for spatial variations, we treat the "Solar" continuum and associated 3.5 keV and 4.5 keV lines as if they had an instrumental origin and thus should only vary between detectors and not within them. Although this treatment amounts to a very coarsely defined spatial model, this component is typically only important below 5 keV where sources are brightest. We note, however, that X-ray emission from the Sun is highly variable and that during flares this component can dominate up to 10 keV; such periods are not currently handled by the background model described here, since the spectrum itself is likely to evolve from the quiescent one we include. When data are split between the periods that the spacecraft is and is not illuminated by the Sun, the correlation between the soft emission and a solar origin is clear, as shown in the examples in Figure 12, the four panels of which also demonstrate its variability.

In contrast, the components of the background with an instrumental origin should not depend on position within the FOV, as long as the detectors are all uniform and identical. Consisting of single CdZnTe crystals, each individual detector should be very close to uniform, which agrees with the lack of spatial fluctuations across any given detector in the stacked high energy images of the blank sky fields. The detectors are not identical, however, and the variation between them in thickness and charge transport properties lead to slight differences in overall background level and line strengths. For any given observation, the overall level and strengths depend on the orbital history through the SAA and other higher radiation zones. Since all the detectors share this history, the *relative* strengths of the internal components

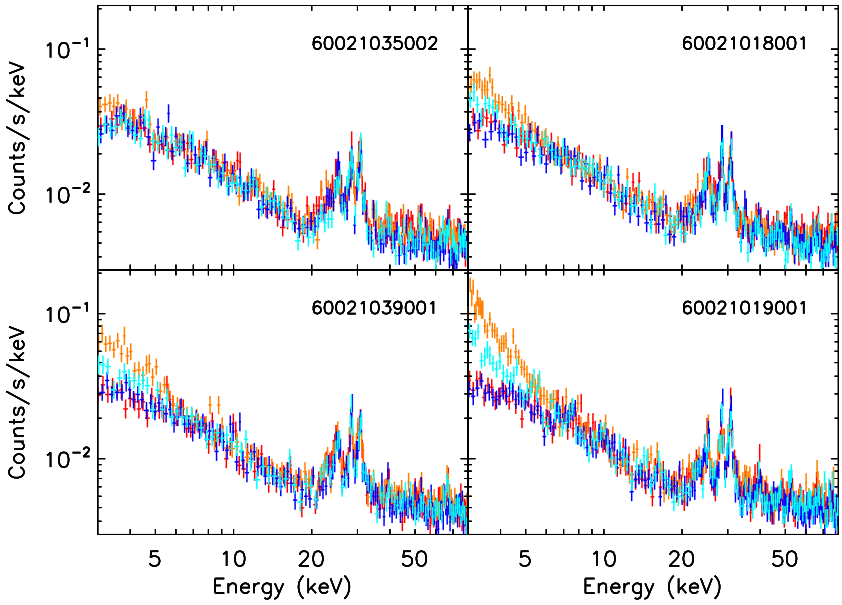

Figure 12. Four observations of COSMOS fields, with the data from each telescope separated into periods when the spacecraft is in the Earth's shadow (A: red; B: blue) and when it is illuminated by the Sun (A: orange; B: cyan). These spectra show how fluctuations in solar activity can increase the low energy background, and that more reflected solar emission is apparently visible to A.

(A color version of this figure is available in the online journal.)

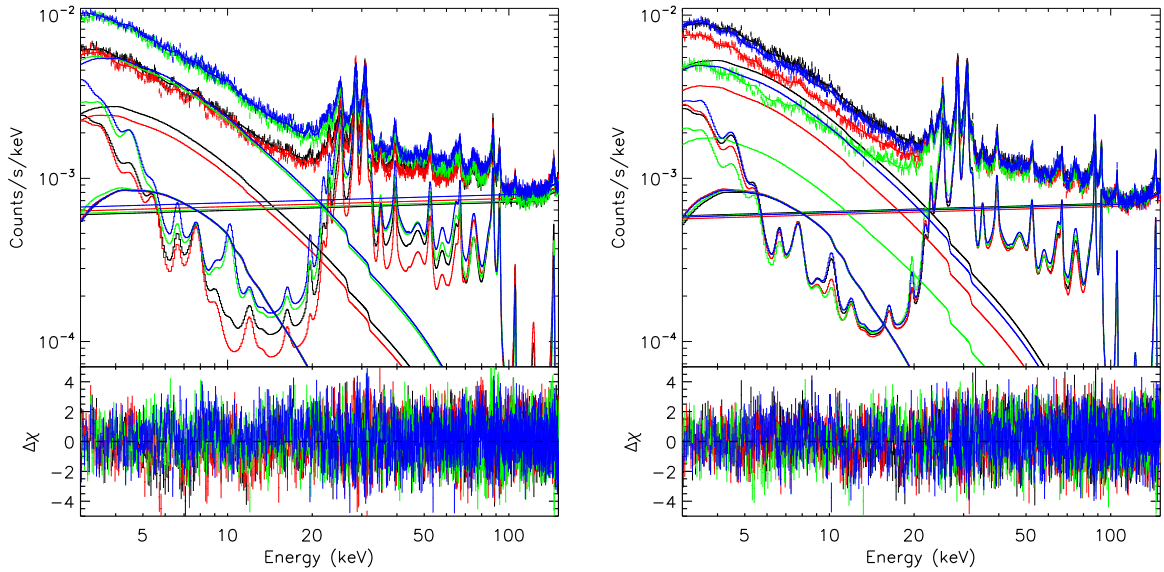

Figure 13. Background model fit to the blank sky spectra from focal planes A (left panel) and B (right panel), separated by detector: Det0 (black), Det1 (red), Det2 (green), and Det3 (blue). The spectral shapes of each component are fixed, but the normalizations are free to vary to account for differences between detectors.

(A color version of this figure is available in the online journal.)

should always be the same. To complete our empirical spectro-spatial model of the background, we simply need to determine the ratios between these components for the detectors on each of the two focal planes. We separate each full FOV spectrum from Figure 10 into four spectra corresponding to each detector, which each share the same spectral model shapes. Having previously determined the "Aperture" and "fCXB" model spatial shapes, the relative proportion of their flux falling on each detector is fixed appropriately, but all other model normalizations are left free. The four spectra are then fit simultaneously, and independently for each telescope, and the resulting fits are shown in Figure 13. Decomposing $I_d(E)$ into independent lines and treating spatial differences as normalizations between detectors, Equation (1) becomes

$$B_d(E) = a_0(a_d/a_0)A(E) + f(E) + s_d S(E) + c_d I_{\rm cont}(E) + \sum_l L_{d,l} \frac{w_l/2\pi}{(E-E_l)^2 + (w_l/2)^2}, \quad \text{(A1)}$$

where the constants a_0, s_d, c_d, and $L_{d,l}$ are free parameters and the spectral shapes given by $A(E)$, $f(E)$, $S(E)$, E_l, w_l, and the ratios a_d/a_0 are fixed. The parameters E_l and w_l give the line centers and widths of the Lorentzian profiles. Many of the lines have similar strengths on each detector, but that is not universally true. Table 4 gives the relative values (normalized to 1 across all four detectors) of the s_d, c_d, and $L_{d,l}$ terms as well

Table 4
Instrumental and Solar Model Parameters

Line Parameters		Telescope A				Telescope B			
Energy (keV)	Width (keV)	Det0	Det1	Det2	Det3	Det0	Det1	Det2	Det3
3.54	0.43	0.217	0.228	0.326	0.228	0.235	0.231	0.209	0.324
4.51	0.54	0.165	0.141	0.393	0.301	0.305	0.219	0.157	0.319
10.20	0.64	0.035	0.000	0.425	0.540	0.308	0.194	0.148	0.350
19.65	0.23	0.295	0.057	0.220	0.427	0.167	0.156	0.407	0.270
21.89	0.57	0.182	0.140	0.248	0.430	0.179	0.259	0.330	0.232
22.97	0.15	0.257	0.204	0.235	0.305	0.230	0.228	0.311	0.231
24.75	1.96	0.204	0.166	0.273	0.357	0.225	0.248	0.290	0.237
25.30	0.15	0.316	0.256	0.231	0.198	0.250	0.245	0.279	0.226
27.75	1.71	0.543	0.457	0.000	0.000	0.232	0.252	0.265	0.251
28.08	2.06	0.000	0.000	0.511	0.489	0.250	0.250	0.250	0.250
28.55	0.27	0.285	0.310	0.195	0.210	0.266	0.251	0.244	0.239
30.17	0.71	0.222	0.182	0.281	0.315	0.245	0.220	0.277	0.257
30.86	0.45	0.273	0.272	0.235	0.220	0.248	0.259	0.255	0.238
32.19	0.86	0.236	0.201	0.259	0.304	0.267	0.250	0.244	0.239
35.03	0.82	0.249	0.277	0.277	0.198	0.265	0.255	0.227	0.254
39.25	9.13	0.238	0.150	0.299	0.313	0.252	0.235	0.253	0.260
39.40	0.52	0.231	0.215	0.234	0.320	0.225	0.239	0.269	0.267
47.56	6.82	0.261	0.193	0.286	0.260	0.246	0.252	0.245	0.256
52.50	1.60	0.241	0.193	0.260	0.306	0.233	0.245	0.266	0.256
57.99	4.72	0.237	0.162	0.257	0.345	0.247	0.255	0.233	0.265
65.01	5.24	0.230	0.162	0.270	0.338	0.228	0.218	0.271	0.283
67.06	0.53	0.233	0.279	0.193	0.296	0.278	0.267	0.210	0.245
75.18	5.59	0.204	0.300	0.191	0.305	0.242	0.205	0.259	0.294
85.82	7.58	0.219	0.236	0.274	0.271	0.274	0.241	0.260	0.225
87.90	0.58	0.299	0.279	0.199	0.223	0.241	0.260	0.238	0.260
92.67	0.64	0.279	0.282	0.210	0.228	0.242	0.257	0.247	0.254
105.36	0.46	0.272	0.335	0.172	0.221	0.237	0.246	0.238	0.279
122.74	2.30	0.275	0.458	0.076	0.192	0.204	0.261	0.263	0.272
144.56	0.74	0.300	0.294	0.193	0.213	0.253	0.260	0.229	0.258
Solar		0.222	0.189	0.216	0.373	0.279	0.262	0.195	0.264
Int. cont.		0.239	0.252	0.243	0.266	0.254	0.244	0.252	0.250

as the values of E_l and w_l. Also, we find indices for the $I_{\rm cont}(E)$ term of -0.05 and -0.85 below and above the break energy of 124 keV and `APEC` temperature and abundance relative to solar values for the $S_d(E)$ term of 1.15 keV and 1.33, respectively.

Based on the above description, each identified component making up *NuSTAR*'s background has been assigned a fixed spectral shape and spatial distribution across the FOV. Given these assumptions, one can directly measure a "local" background for any subset of the FOV and use that to accurately predict the background for anywhere in the entire FOV. The quality of the background is of course limited by the statistics available in the observation used to constrain the background model, but one advantage of separating out the different components is that separate systematic uncertainties associated with each component can be applied individually.

APPENDIX B

APPLICATION OF THE BACKGROUND MODEL: `nuskybgd`

B.1. Determining the Background of the Bullet Cluster Observations

Now that we have a background model, we can use the events far from the cluster to determine the precise level of each background component, which are unique to the conditions of these observations. To apply the model defined in Appendix A, we have developed a small suite of IDL routines called `nuskybgd`, whose purpose is to take regions defined in sky coordinates, compute the relative strengths of each background component based on their location in the detector plane, and create an `XSPEC`-readable script that sets up and fits for all observation-specific component normalizations, much in the spirit of the background treatment in the *XMM-Newton* Extended Source Analysis Software package (as introduced in Snowden et al. 2008). Those normalizations correspond to a complete spectro-spatial background model from which images in any energy band or spectra for any region can be produced.

In principle, we could extract a single spectrum of the non-cluster part of the FOV for each telescope and epoch and fit the model to that. The downside of this approach is that all spatial information is lost, which can cause the various components—especially the "Aperture" component—to obtain unphysical best-fit normalizations. To incorporate this information while also keeping the computational load to a minimum, we divide the non-cluster area into four rectangular regions for each focal plane and epoch, shown in Figure 14. We also try to minimize the "contamination" of these regions with cluster emission, mostly originating from the brightest parts of the cluster and carried far away from its true location by the wings of the PSF. The ellipse in Figure 14 indicates the parts of the background regions excluded for this reason. Even so, residual cluster emission remains, which we must also model to avoid biasing the background model.

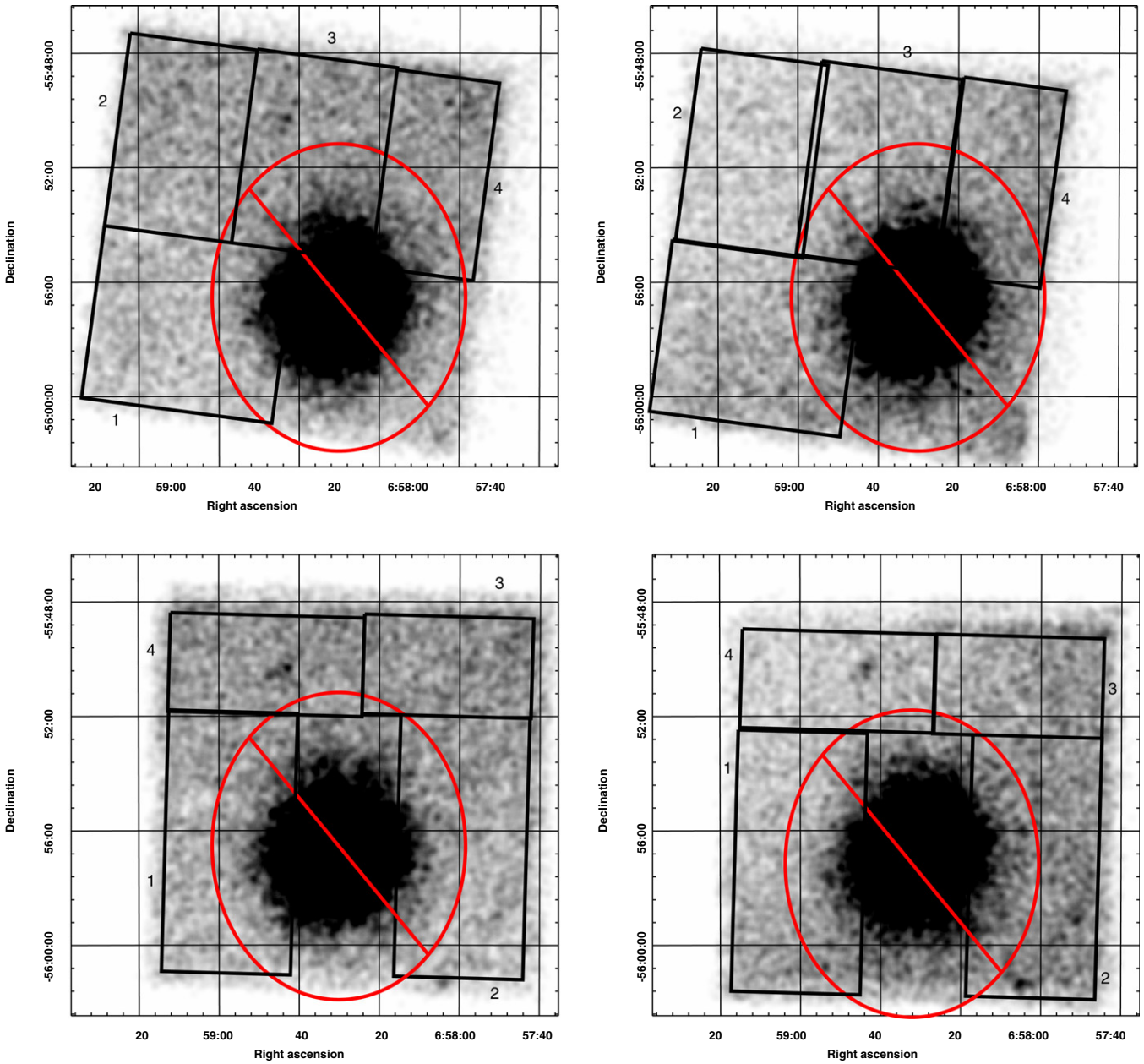

Figure 14. Regions from which spectra are extracted to characterize the background; events inside the ellipse are excluded. Data from telescopes A and B are shown in the left and right panels, and the first and second epochs are shown in the top and bottom panels, respectively. The data are the same as in Figure 1: the images have been smoothed by Gaussian kernel of width 5 pixels and scaled between 0 (white) and 1 (black) counts to bring out structure in the background.

(A color version of this figure is available in the online journal.)

For the most part, the regions from each telescope and epoch are fit independently, but the CXB components between telescopes and epochs are correlated and can be tied together to improve their precision. The "fCXB" component, being the unresolved contribution of sources in that region of the sky, will be identical for telescopes A and B as long as the regions are roughly coincident. Similarly, because the roll angle is very similar between the two epochs, the part of the sky producing the "Aperture" component for each telescope is almost entirely identical. Fitting all 16 spectra simultaneously therefore permits the normalizations of these parameters to be appropriately tied together, reducing the number of free parameters and the chance that any component gets pushed to an unphysical value by preventing the fit from heading down a local minimum. We pursue this strategy because below ∼15 keV all of the background components contribute at non-negligible levels, making it easier for the fit minimization procedure to be misled by mere statistical fluctuations.

Despite having a conservative exclusion region around the cluster, a small but noticeable number of cluster photons are scattered into the background regions, roughly at the level of the "fCXB" component. Because its contribution is fairly modest, the spectral model used to account for its emission does not have to be extremely accurate; we take a single temperature model at the global average temperature of 14.1 keV and abundance relative to solar of 0.15 convolved with the same ARF used by the "fCXB" component. The spectral shapes and normalizations of the scattered cluster emission and "fCXB" components turn out to be very similar, which means that if both were left free they may very well take on unphysical values. Even under these

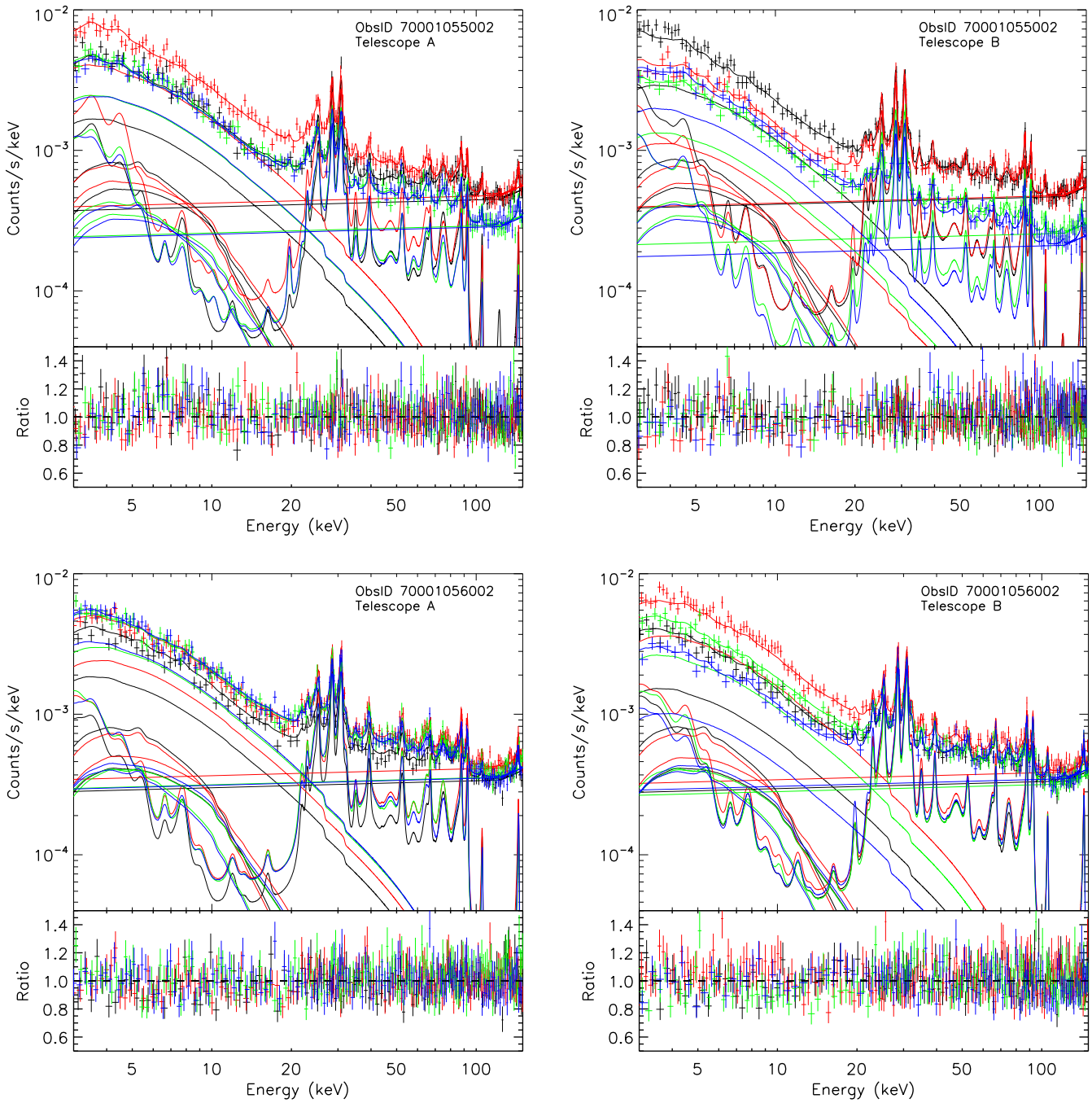

Figure 15. Simultaneous fit of the model background to the 16 spectra extracted from the regions shown in Figure 14, with the spectra in each panel associated with a single observation and focal plane as labeled; the black, red, green, and blue data (crosses) and model components (lines) correspond to regions 1, 2, 3, and 4, respectively, as labeled in Figure 14. We fit the two epochs together primarily so that the "Aperture" component can be described by only one free parameter, consistent with the nature of its origin.

(A color version of this figure is available in the online journal.)

circumstances, however, the overall background model should not suffer, since the scattered component is not included in it and the "fCXB" normalization, while on average constant across the FOV, can significantly vary location-to-location due to cosmic variance. As that flux in the background regions cannot be directly applied at the cluster location, we simply fix the "fCXB" component to its average value and allow the scattered cluster emission component to be free, which may compensate for variations in the CXB flux in each region as well. The fit to all background region spectra is shown in Figure 15. The "fCXB" normalizations are simply scaled for each region assuming the *HEAO-1*-measured CXB flux (Boldt 1987), and the "Aperture" normalizations were found to be factors of 0.993 and 1.018 of this flux for A and B, respectively. We provide the values of the s_0, c_0, and $L_{0,l}$ terms for the A and B background of both observations in Table 5.

B.2. Applying the Background Model to the Bullet Cluster Spectra

The background model is defined both spatially and spectrally, and its parameters have now been determined for our

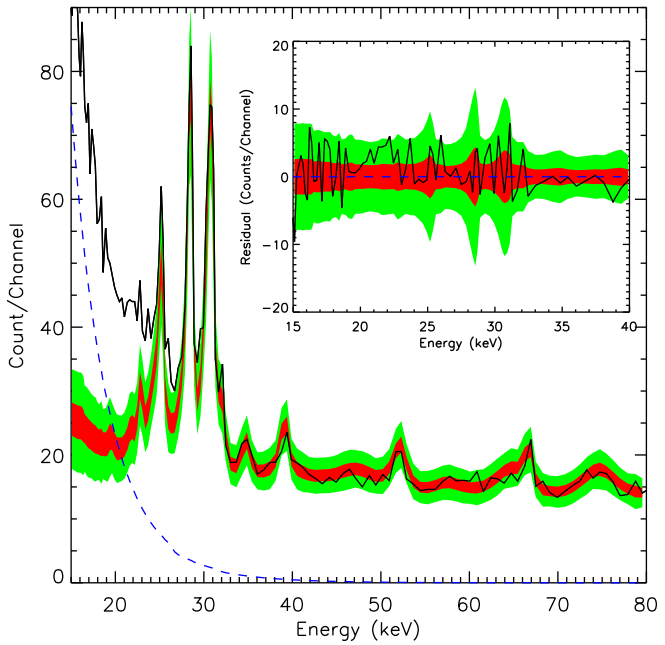

Figure 16. Bullet cluster spectrum at hard energies (solid line) is shown with the 1σ (red; dark gray) and 3σ (green; light gray) ranges given by the 1000 background realizations. The dashed (blue) line indicates the average 1T thermal model contribution to the spectrum. The inset plot gives the residual of the fit to the thermal model after background subtraction, with the same shaded regions displayed in the main plot illustrating the extent of fluctuations expected from the background alone. While the nominal background model appears too low just above 20 keV and too high from ∼35–55 keV, it is clear these variations are not extreme.

(A color version of this figure is available in the online journal.)

specific observations, allowing a background spectrum to be generated from the model for any location in the FOV with `nuskybgd`. To realistically assess the impact of both statistical and systematic uncertainties associated with the background on fits to the cluster spectrum, we perform Monte Carlo simulations of the background including those uncertainties as fluctuations from the expected model. Because the background is broken up into separate components, each one can be varied based on its own systematic error, as specified in Section 3.1.2. Each of the simulated background spectra is generated in two steps from the predicted model for the source region. First, the normalizations of each component are randomly shifted, assuming a normal distribution about their systematic uncertainty. Then, a counts spectrum with Poisson fluctuations is created from the adjusted model for an exposure time equal to that of the observation using the `fakeit` command in `XSPEC`. While counting statistics should not bias the modeling of the Bullet cluster spectrum in principle, the true background can be thought of as one such realization; a conspiracy of high or low shot noise at just the right energies would act just like a systematic offset. Our procedure captures the likelihood of such occurrences and thus more realistic error ranges for the cluster model parameters.

We simulate 1000 background spectra, enough to characterize the standard deviation at each energy and confirm the naive expectation that the fluctuations are roughly Gaussian out to $\sim 3\sigma$. Considering the full gamut of likely background spectra, as opposed to the nominal model derived from local background regions, puts several intriguing or worrying features in the proper context. In Figure 16, the hard band of the Bullet cluster spectrum is shown relative to the range bound by the background simulations (red/green or gray shaded regions) and relative

Table 5
Bullet Cluster Instrumental and Solar Model Parameters for Detector 0

	70001055002		70001056002	
	A	B	A	B
E_l (keV)	$L_{0,l}$ Normalizations[a] (photons s^{-1} cm^{-2})			
3.54	2.47E-03	5.53E-04	1.55E-03	1.44E-03
4.51	1.15E-03	2.24E-03	8.20E-04	2.64E-03
10.20	8.41E-08	3.58E-15	4.76E-06	3.41E-04
19.65	2.04E-04	9.78E-05	3.65E-10	1.22E-04
21.89	1.17E-04	4.95E-04	3.30E-04	1.81E-04
22.97	4.51E-04	3.20E-04	4.59E-04	6.45E-04
24.75	3.22E-03	2.54E-03	2.88E-03	2.85E-03
25.30	1.07E-03	1.24E-03	1.20E-03	1.15E-03
27.75	1.41E-03	2.28E-03	1.83E-03	2.04E-03
28.08	1.07E-16	6.61E-20	1.25E-16	6.81E-20
28.55	3.89E-03	4.22E-03	3.81E-03	4.10E-03
30.17	1.28E-03	6.60E-04	1.29E-03	1.20E-03
30.86	5.00E-03	4.91E-03	5.07E-03	4.58E-03
32.19	1.44E-03	1.86E-03	1.24E-03	2.07E-03
35.03	7.45E-04	1.00E-03	6.17E-04	1.28E-03
39.25	5.20E-03	4.90E-03	5.56E-03	4.61E-03
39.40	7.86E-04	7.70E-04	1.03E-03	8.42E-04
47.56	3.54E-03	3.87E-03	3.88E-03	4.43E-03
52.50	1.77E-03	1.51E-03	2.28E-03	1.42E-03
57.99	1.70E-03	1.83E-03	1.82E-03	1.54E-03
65.01	3.89E-03	2.93E-03	4.04E-03	3.17E-03
67.06	4.23E-04	6.27E-04	7.68E-04	1.12E-03
75.18	4.11E-03	3.53E-03	4.46E-03	3.75E-03
85.82	4.12E-03	4.16E-03	4.15E-03	4.88E-03
87.90	2.23E-03	2.40E-03	2.44E-03	2.20E-03
92.67	2.41E-03	2.37E-03	2.52E-03	2.97E-03
105.36	1.26E-03	8.31E-04	8.77E-04	1.05E-03
122.74	9.11E-04	5.47E-04	2.21E-04	4.35E-04
144.56	4.95E-03	3.82E-03	4.43E-03	4.77E-03
s_0[b]	1.16E-01	3.46E-01	1.91E-01	3.14E-01
c_0[c]	5.52E-04	5.64E-04	5.60E-04	5.68E-04

Notes.
[a] For instrumental lines only.
[b] For "solar" component, `APEC` norm.: $\{10^{-14}/[4\pi(1+z)^2 D_A^2]\} \int n_e n_{\rm H}\, dV$, where z is the redshift, D_A is the angular diameter distance, n_e is the electron density, $n_{\rm H}$ is the ionized hydrogen density, and V is the volume of the cluster.
[c] For instrumental continuum component, broken power-law norm.: photons s^{-1} cm^{-2} keV^{-1} at 1 keV.

to the average 1T thermal model (blue/dashed line). Above ∼50 keV, the spectrum generally agrees well with the mean expectation of the background, and deviations from the mean fall appropriately distributed within the range. A few energy ranges, however, show more systematic deviations from the mean. From ∼20–22 keV, the spectrum quickly rises above the 1T model, and from ∼35–50 keV the spectrum stays slightly, but consistently, below the mean background level. When considered relative to the allowed range of the background, it is clear that the deviations are not worryingly extreme. A common systematic fluctuation in the 35–50 keV background could cause the $\sim 1\sigma$ offset, and the blip at 22 keV is most likely an imperfectly calibrated background line or lines (see Table 4).

REFERENCES

Ajello, M., Rebusco, P., Cappelluti, N., et al. 2009, ApJ, 690, 367
Ajello, M., Rebusco, P., Cappelluti, N., et al. 2010, ApJ, 725, 1688
Andersson, K., Peterson, J. R., & Madejski, G. 2007, ApJ, 670, 1010
Barcons, X., Mateos, S., & Ceballos, M. T. 2000, MNRAS, 316, L13

Boldt, E. 1987, in IAU Symposium, Vol. 124, Observational Cosmology, ed. A. Hewitt, G. Burbridge, & L. Z. Fang (Cambridge: Cambridge Univ. Press), 611
Bonafede, A., Feretti, L., Murgia, M., et al. 2010, A&A, 513, A30
Bonamente, M., Nevalainen, J., & Lieu, R. 2007, ApJ, 668, 796
Clarke, T. E., Kronberg, P. P., & Böhringer, H. 2001, ApJL, 547, L111
Govoni, F., & Feretti, L. 2004, IJMPD, 13, 1549
Govoni, F., Markevitch, M., Vikhlinin, A., et al. 2004, ApJ, 605, 695
Harrison, F. A., Craig, W. W., Christensen, F. E., et al. 2013, ApJ, 770, 103
Humphrey, P. J., Liu, W., & Buote, D. A. 2009, ApJ, 693, 822
Keshet, U., Kushnir, D., Loeb, A., & Waxman, E. 2012, arXiv:1210.1574
Kim, K.-T., Kronberg, P. P., Dewdney, P. E., & Landecker, T. L. 1990, ApJ, 355, 29
Kim, M., Wilkes, B. J., Kim, D.-W., et al. 2007, ApJ, 659, 29
Kushnir, D., & Waxman, E. 2010, JCAP, 02, 025
Leccardi, A., & Molendi, S. 2007, A&A, 472, 21
Lehto, T., Nevalainen, J., Bonamente, M., Ota, N., & Kaastra, J. 2010, A&A, 524, A70
Liang, H., Hunstead, R. W., Birkinshaw, M., & Andreani, P. 2000, ApJ, 544, 686
Markevitch, M. 2006, in The X-ray Universe 2005, ed. A. Wilson (ESA SP-604; Noordwijk: ESA), 723
Markevitch, M., Gonzalez, A. H., David, L., et al. 2002, ApJL, 567, L27
Markwardt, C. B. 2009, in ASP Conf. Ser. 411, Astronomical Data Analysis Software and Systems XVIII, ed. D. A. Bohlender, D. Durand, & P. Dowler (San Francisco, CA: ASP), 251
Mewe, R., Kaastra, J. S., & Liedahl, D. A. 1995, Legacy, 6, 16
Mitchell, R. J., Culhane, J. L., Davison, P. J. N., & Ives, J. C. 1976, MNRAS, 175, 29
Moretti, A., Gastaldello, F., Ettori, S., & Molendi, S. 2011, A&A, 528, A102
Nevalainen, J., David, L., & Guainazzi, M. 2010, A&A, 523, A22
Nynka, M., Hailey, C. J., Mori, K., et al. 2013, ApJL, 778, L31
Ota, N., Nagayoshi, K., Pratt, G. W., et al. 2014, A&A, 562, A60
Petrosian, V., Madejski, G., & Luli, K. 2006, ApJ, 652, 948
Rephaeli, Y. 1979, ApJ, 227, 364
Rephaeli, Y. 1987, MNRAS, 225, 851
Rephaeli, Y., & Gruber, D. E. 1988, ApJ, 333, 133
Rephaeli, Y., Nevalainen, J., Ohashi, T., & Bykov, A. M. 2008, SSRv, 134, 71
Revnivtsev, M., Gilfanov, M., Sunyaev, R., Jahoda, K., & Markwardt, C. 2003, A&A, 411, 329
Shafer, R. A. 1983, PhD thesis, Univ. Maryland
Snowden, S. L., Mushotzky, R. F., Kuntz, K. D., & Davis, D. S. 2008, A&A, 478, 615
Solinger, A. B., & Tucker, W. H. 1972, ApJL, 175, L107
Thierbach, M., Klein, U., & Wielebinski, R. 2003, A&A, 397, 53
Tucker, W., Blanco, P., Rappoport, S., et al. 1998, ApJL, 496, L5
Türler, M., Chernyakova, M., Courvoisier, T. J.-L., et al. 2010, A&A, 512, A49
Wik, D. R., Sarazin, C. L., Finoguenov, A., et al. 2009, ApJ, 696, 1700
Wik, D. R., Sarazin, C. L., Zhang, Y.-Y., et al. 2012, ApJ, 748, 67
ZuHone, J. A., Markevitch, M., & Lee, D. 2011, ApJ, 743, 16